applied sciences

MDPI

Article

Axial Load Transfer Mechanisms in Fully Grouted Fibreglass Rock Bolts: Experimental and Numerical Investigations

Shima Entezam [1,2,*], Ali Mirzaghorbanali [1,2], Behshad Jodeiri Shokri [1,2], Alireza Entezam [1,2], Hadi Nourizadeh [1,2], Peter Craig [3], Kevin McDougall [4], Warna Karunasena [1,2] and Naj Aziz [5]

[1] School of Engineering, University of Southern Queensland, Springfield Central, QLD 4300, Australia; ali.mirzaghorbanali@unisq.edu.au (A.M.); behshad.jodeirishokri@unisq.edu.au (B.J.S.); alireza.entezam@unisq.edu.au (A.E.); hadi.nourizadeh@unisq.edu.au (H.N.); karu.karunasena@unisq.edu.au (W.K.)
[2] Centre for Future Materials (CFM), University of Southern Queensland, Toowoomba, QLD 4350, Australia
[3] Jennmar Australia Pty. Ltd., Sydney, NSW 2567, Australia; pcraig@jennmar.com.au
[4] School of Surveying and Built Environment, University of Southern Queensland, Toowoomba, QLD 4350, Australia; kevin.mcdougall@unisq.edu.au
[5] School of Civil, Mining & Environmental Engineering, University of Wollongong, Wollongong, NSW 2500, Australia; naj@uow.edu.au
* Correspondence: shima.entezam@unisq.edu.au; Tel.: +61-424-256-424

Abstract

Fully grouted rock bolts play a vital role in stabilising underground excavations, particularly in corrosive environments where material properties, geometric configuration, and installation conditions influence their load transfer performance. Although the practical importance of fully grouted fibreglass rock bolts is well recognised, quantitative evidence on their axial load transfer mechanisms remains limited. Prior work has primarily centred on steel rock bolts, with few studies on how embedment length, grout stiffness, interface roughness and confining stress govern bond mobilisation in fully grouted fibreglass rock bolts, indicating a clear need for further scientific investigation. This study examines the axial load transfer and shear behaviour of fully grouted fibreglass rock bolts, focusing on the effects of embedment length (EL), grout properties, and boundary conditions. A comprehensive series of laboratory pull-out tests were conducted on two widely used Australian glass fibre reinforced polymer (GFRP) rock bolts, TD22 and TD25, with diameters of 22 mm and 25 mm, respectively, under varying ELs and grout curing times to evaluate their axial performance. Additionally, single shear tests and uniaxial compressive strength (UCS) tests were conducted to assess the shear behaviour of the rock bolts and the mechanical properties of the grout. The results showed that increased EL, bolt diameter, and grout curing time generally enhance axial capacity. With grout curing from day 7 to the day 28, the influence of embedment length became increasingly pronounced, as the axial peak load rose from 35 kN (TD22-50, 7 days) to 116 kN (TD22-150, 28 days) and from 39 kN (TD25-50, 7 days) to 115 kN (TD25-150, 28 days), confirming that both longer bonded lengths and extended curing significantly enhance the axial load-bearing capacity of fully grouted GFRP rock bolts. However, the TD22 rock bolts exhibited superior shear strength and ductility compared to the TD25 rock bolts. Also, a calibrated distinct element model (DEM) was developed in 3DEC to simulate axial load transfer mechanisms and validated against experimental results. Parametric studies revealed that increasing the grout stiffness from 5 e7 N/m to 5 e8 N/m increased the peak load from 45 kN to 205 kN (approximately 350%), while reducing the peak displacement, indicating a shift toward a more brittle response. Similarly, increasing the grout-bolt interface roughness boosted the peak load by 150% (from 60 kN to 150 kN) and enhanced

Academic Editors: Yong Zhao and Tianhong Yang

Received: 18 September 2025
Revised: 8 October 2025
Accepted: 17 October 2025
Published: 21 October 2025

Citation: Entezam, S.; Mirzaghorbanali, A.; Jodeiri Shokri, B.; Entezam, A.; Nourizadeh, H.; Craig, P.; McDougall, K.; Karunasena, W.; Aziz, N. Axial Load Transfer Mechanisms in Fully Grouted Fibreglass Rock Bolts: Experimental and Numerical Investigations. *Appl. Sci.* **2025**, *15*, 11293. https://doi.org/10.3390/app152011293

Copyright: © 2025 by the author. Licensee MDPI, Basel, Switzerland. This article is an open access article distributed under the terms and conditions of the Creative Commons Attribution (CC BY) license (https://creativecommons.org/licenses/by/4.0/).

residual stability, raising the residual load from 12 kN to 93.5 kN. In contrast, confining stress (up to 5 MPa) did not affect the 110 kN peak load but reduced the residual load by up to 60% in isotropic conditions. These quantitative findings provide critical insights into the performance of GFRP bolts and support their optimised design for underground reinforcement applications.

Keywords: fibreglass rock bolts; axial load transfer mechanism; distinct element modelling (DEM); grout stiffness; interface roughness; confining stress

1. Introduction

Underground excavations, such as tunnels, mine roadways, and caverns, inevitably disturb the in situ stress regime, resulting in the redistribution of the loads and inducing deformations around the exposed boundary [1]. If not controlled, these disturbances often lead to instability and a progressive failure mechanism in the surrounding rock mass. Reinforcement systems, particularly rock bolts, have therefore become a fundamental component of ground support design in both mining and civil engineering projects. In general, rock bolts restrain displacements, enhance the self-supporting capacity of the rock mass, and help maintain the integrity of underground structures [2].

Rock bolting systems are usually classified by the way the load is transferred from the tendon to the rock mass [3]. The three principal groups are continuously mechanically coupled (CMC), continuously frictionally coupled (CFC), and discretely mechanically or frictionally coupled (DMFC) systems [4]. Within this framework, fully grouted rock bolts, a CMC system, are widely used in the industry. Their popularity arises from simple installation, wide material availability, and relatively low cost compared to alternatives [5]. A fully grouted rock bolt typically consists of a steel or composite bolt element installed in a borehole and bonded with either cementitious grout or resin. When the rock mass deforms, the bolt element is loaded axially in tension, and shear stresses mobilised at the grout-bolt interface transmit this load into the surrounding rock [4]. Two anchor models underpin today's understanding of fully grouted rock bolting systems, including Farmer's shear-stress decay solution for resin-grouted anchors and Li & Stillborg's interface model, which admits elastic-softening-debonding zones [6,7]. Standard experimental tests for characterising axial and shear behaviour include pull-out [8]/push-out tests [9] and single/double shear tests [10,11]. Findings of such studies showed that axial load transfer in fully grouted rock bolts is governed by the development of shear resistance at the bolt-grout interface and the axial force distribution along the bolt element [12]. Factors controlling bond and axial load transfer in fully grouted systems include [13]: (1) rock bolt geometry and rib profile, which regulate mechanical interlock and radial dilation; (2) grout type and stiffness/strength; (3) borehole diameter and annulus; (4) confinement/host rock stiffness and jointing; and (5) boundary conditions (CNL/CNS). Recent studies have refined these dependencies using combined testing and modelling. For example, rib profile effects and interface shear [14], progressive debonding under axial loading [15], micromechanical modelling of debonding/damage [16], and grout composition effects [17].

The geometry of the rock bolt element, including rib height, spacing, and angle, has long been recognised as critical in controlling bond behaviour. Constant normal load (CNL) and constant normal stiffness (CNS) tests reveal how different rib profiles influence both peak and residual bond capacity. Laboratory investigations by Cui et al. highlighted the effect of bolt profiles under CNS conditions [14]. At the same time, Zhang et al. quantified the role of grout mixture and rib geometry under CNL loading [18].

Subsequent work by Wang et al. (2022) incorporated more realistic rib geometries and demonstrated strong dependency on boundary stiffness [19]. More recently, Zhang et al. showed how rib spacing and angle govern the transition from interfacial slip to pull-out failure [20]. Micromechanical modelling confirms that these parameters interact with grout strength to shape damage localisation [21].

A recurring design parameter is the critical/optimum embedment length (EL) required to mobilise bond without interface debonding or bolt element rupture. For steel rock bolts, modern pull-out studies calibrate EL against grout/host rock properties and rib geometry. A recent synthesis and testing programme on grouted rock bolts quantified the relation between EL and bond strength and its sensitivity to confinement and grout [22]. In another research, Li et al. introduced the concept of a critical EL by evaluating various water-to-grout (W/G) ratios, demonstrating that variations in EL can directly influence the bond strength [23]. Similarly, Yu and Zhu reported that increasing the EL enhances the axial capacity of the rock bolt system as a result of the corresponding rise in bond strength [24].

In addition to geometry, embedment length (EL), and boundary conditions, the grout plays a crucial role in determining the axial response of rock-bolting systems [25]. In fact, the grout medium is not simply passive, but actively controls the stiffness, load transfer, and post-peak behaviour of the rock bolting system. Hu et al. showed that elevated temperatures accelerate bond degradation between grouting materials and the anchorage system in high-geothermal tunnels [26]. Numerical modelling frameworks now capture these phenomena, coupling finite-discrete methods to represent rib-scale fracture and bond-slip [27]. Large-scale work has drawn attention to the quality of grouting. Thirukumaran et al. proposed acceptance metrics for in situ pull-out testing to evaluate bond integrity between grout and the rock bolting system [28].

Corrosion and chemical attacks also compromise the long-term performance of the rock bolting systems. Recent studies document stress-corrosion cracking and bond deterioration in steel rock bolts [29]. Conventional steel rock bolts are effective due to their superior tensile strength and ductile behaviour [3], but they are vulnerable to corrosion, particularly in humid, saline, or chemically aggressive environments [30]. In fact, the thermo-electrochemical processes occurring in such environments can induce void formation and cracking within the grout medium, progressively reducing the steel's cross-sectional area and generating stress concentrations that may ultimately lead to failure of the rock bolting systems [31]. Protective coatings such as epoxy may delay deterioration but are not always reliable in chloride-rich environments [32]. Fibre-reinforced polymer (FRP) rock bolts, and, in particular, glass fibre reinforced polymer (GFRP) rock bolts, have therefore gained traction as alternatives. Comparative studies between fibreglass and steel rock bolts have shown that fibreglass rock bolts can achieve up to approximately 85% of the ultimate tensile strength of the steel rock bolts [11,33]. Indeed, GFRP rock bolts combine corrosion resistance, cuttability and light weight with high tensile strength along the fibre axis [11]. Recent tunnel applications have confirmed that GFRP can mobilise bond stiffness comparable to that of steel rock bolts under certain conditions [34–38]. Early pull-out experiments showed that fully grouted GFRP rock bolts can develop robust bond [39]. Numerical modelling of tunnel faces reinforced with GFRP rock bolts also indicated reductions in extrusion displacements [40]. Sustainability assessments reinforce these advantages. FRP tendon can lower life-cycle impacts compared to steel [41] and reduce carbon emissions by approximately 40% compared to traditional steel reinforcement bars [42]. Despite these benefits, GFRP rock bolts differ from steel rock bolts in terms of stiffness, which influences both axial and shear load transfer. Gregor investigated the influence of pretension on the shear behaviour of fully grouted GFRP rock bolts across clean and infilled joints using a modified double-shear test configuration and found that

pretensioned GFRP rock bolts exhibited greater shear capacity than their untensioned system [43]. This work was further modelled and validated by developing analytical models and simulating three-dimensional scenarios using FLAC3D [44].

Although significant advances have been made in steel rock bolting systems and, more recently, in GFRP systems, the axial load-transfer behaviour of fully grouted fibreglass rock bolts remains insufficiently characterised, particularly regarding the combined influence of EL and grout stiffness under realistic boundary conditions. Previous research has demonstrated the critical role of EL in fully grouted steel rock bolting systems [22], but the systematic investigation of these parameters in fibreglass rock bolts remains limited. To address this gap, the present study integrates a series of systematic laboratory pull-out tests on two Australian fibreglass rock bolt types with developing numerical modelling in the three-dimensional distinct element code (3DEC), where the pile structural element is used to simulate axial-shear coupling and bond-slip behaviour under varied grout and confinement conditions [45]. The scientific problem addressed in this research is the absence of calibrated, design-relevant relations for fully grouted GFRP rock bolts that link EL to axial force transfer and interface debonding. Therefore, the primary objective of this research is to enhance the understanding of how various EL with double-embedment configurations and different curing time ranges influence the axial load transfer mechanism and bond evolution in fully grouted rock bolts through a systematic experimental laboratory pull-out test. Subsequently, a numerical model was developed and validated using the experimental results, followed by a parametric numerical analysis to quantify the effects of (a) grout stiffness, (b) bolt–grout stiffness ratio, and (c) confining stress on the performance of axial load transfer behaviour of fully grouted GFRP rock bolts. Through this combined experimental-numerical approach, the study advances the mechanistic understanding of load transfer in fully grouted GFRP rock bolts, contributing to more reliable and efficient design practices for ground support systems in civil and mining excavations.

2. Materials and Methods

This study followed a structured experimental-numerical scheme to investigate the axial load transfer mechanism of fully grouted GFRP rock bolts. Two Australian-manufactured rock bolts, TD22 and TD25, were selected and prepared with double-embedment configurations under controlled curing times of 7, 14, 21, and 28 days. Material characterisation included uniaxial compressive strength (UCS) testing of the grout and shear testing of the bolts to determine their mechanical properties. These tests provided the fundamental parameters required for later calibration and analysis. Additionally, after designing, preparing, and casting the samples needed, they were subsequently cured in various time intervals. A series of systematic pull-out tests was then conducted to examine the axial behaviour of the fully grouted GFRP rock bolts with different ELs, bolt diameters, and curing times. The resulting load–displacement curves were used to derive key parameters and build a dataset, including peak load, displacement at peak, and axial stiffness. A three-dimensional numerical model was subsequently developed in 3DEC, utilising the pile/rock bolt structural element to simulate the pull-out tests along the fully grouted GFRP rock bolting systems. The model was calibrated against the experimental results and extended through parametric analyses on grout stiffness, grout-rock bolt roughness, and confining stress. This integrated approach allowed a comparison between the laboratory results and the numerical simulations, helping to explain how the mentioned parameters affect axial load transfer in fully grouted GFRP rock bolts. All these steps are shown in Figure 1.

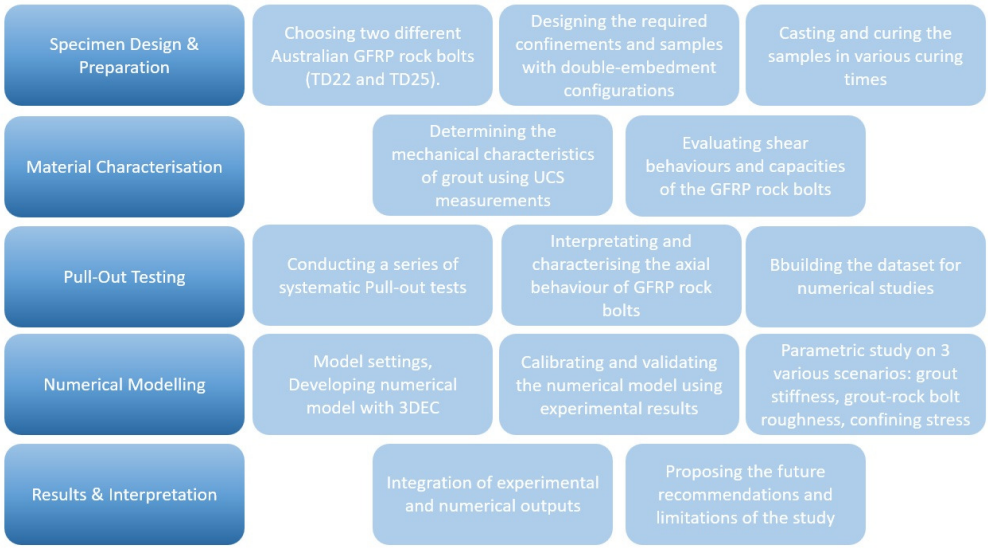


Figure 1. Methodological workflow outlining the experimental and numerical stages of the study.

2.1. Experimental Design

A total of 24 test samples were prepared with different combinations of double-embedding technology for three different Els (50–75 mm), (100–150 mm), and (150–200 mm), four different ranges of curing times ranging from 1 to 28 days, and two different rock bolt diameters, including 22 mm and 25 mm, to capture the effects of these parameters on the axial load-bearing behaviour of the fully grouted GFRP rock bolts. The key geometric configurations of the test samples are given in Table 1.

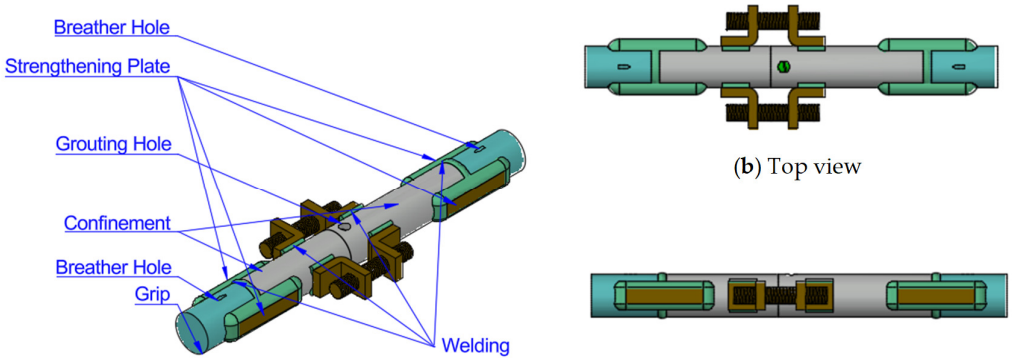
Table 1. Geometry and testing plan for the pull-out tests of the fully grouted GFRP rock bolt samples.

Bolt Type	Bolt Diameter (mm)	Hole Diameter (mm)	Rock Diameter (mm)	Shorter EL (mm)	Longer EL (mm)	Bolt Length (mm)	Curing Time (days)
TD22	22	35	55	50	75	155	7, 14, 21, 28
				100	150	280	
				150	200	380	
TD25	25	35	55	50	75	155	7, 14, 21, 28
				100	150	280	
				150	200	380	

Each sample was secured between two custom-manufactured solid steel grips, allowing it to be clamped into the jaws of the MTS testing machine during pull-out testing. The grips were prepared from 55 mm diameter steel bars, with an overall length of 90 mm. To ensure proper alignment and centring of the GFRP rock bolts, each grip contained a centrally drilled recess measuring 15 mm in depth, with internal diameters of 22.4 mm and 25.4 mm, corresponding to the two bolt types used in the tests. One edge of each grip was chamfered to facilitate a reliable weld connection to the confinement sections.

The confinement components were produced from additional solid steel bars, drilled to a diameter of 35 mm and internally rifled to simulate real field conditions and enhance the bonding interface between the grout and the confinement. The confinement sections were subsequently chamfered on one end to ensure a precise fit, while the opposite end featured a drilled recess to form a male-female connection with the corresponding grip.

Once assembled, each solid bar was welded to its respective confinement section, and two steel plates measuring 20 × 100 mm were welded across the grips to reinforce the assembly and prevent separation under axial pull-out loading. The final sample assembly is shown in Figure 2, illustrating the complete configuration of the test specimen and confinement system.



(**a**) 3D view

(**b**) Top view

(**c**) Side view

Figure 2. Design of the fibreglass rock bolt.

2.2. Materials

The test samples were designed and prepared using three primary materials: steel solid bars for the confinement structure and grips, GFRP rock bolts as the reinforcing element, and a high-strength grout as the bonding medium. Details of each component are outlined below.

2.2.1. Designing and Manufacturing the Required Confinements

Solid bars of 1018/1020 bright mild round steel, (sourced from VULCAN Engineering Steels, Brisbane, Australia) with a diameter of 55 mm, were used to manufacture the confinement sections and grips for the test setup. The solid bars were cut, drilled, rifled, chamfered, and welded to create the confinement system, which was designed to replicate the surrounding rock mass conditions.

To ensure precise alignment of the rock bolt within the confinement, each steel grip was machined with a centralising hole, allowing the rock bolt to sit exactly along the centreline of the assembly. Additional alignment was achieved by drilling two opposing holes on each confinement section, positioned directly across from one another, which provided an apparent reference to confirm that the rock bolt remained correctly centred during preparation (Figures 3 and 4).

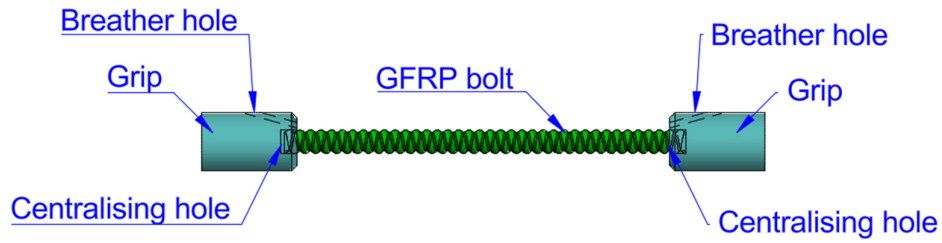


Figure 3. The design of the breather holes, centralising holes and chamfers in the grips.

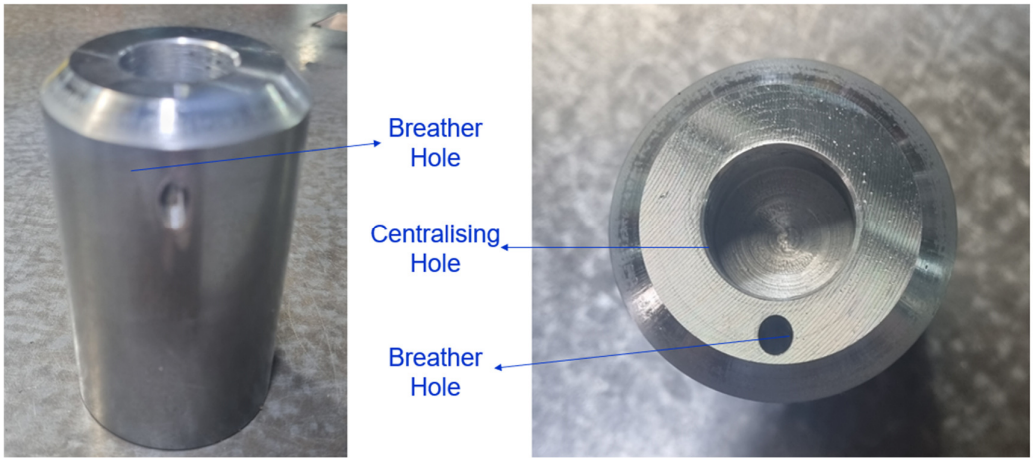


Figure 4. Breather holes, centralising holes and chamfers in the grips.

For grout injection, the system was designed with grouting holes and breather holes. During preparation, grout was pumped into the system through the grouting hole and exited through the breather holes, ensuring the grout filled the entire annulus and completely encapsulated the rock bolt along its whole length inside the confinement (Figure 5). To enhance the bond between the grout and the steel confinement, the internal surfaces were rifled, increasing surface roughness and promoting mechanical interlock (Figure 6).

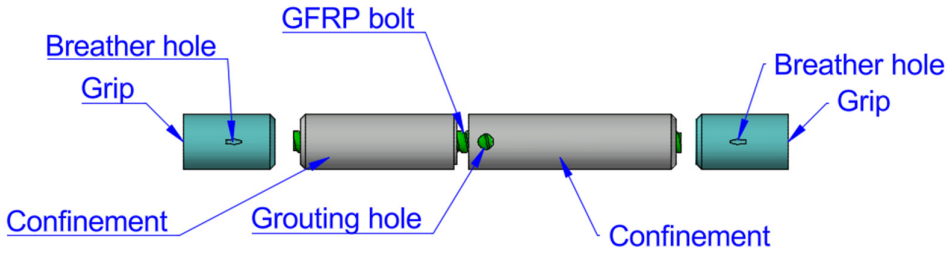


Figure 5. Schematic of the GFRP rock bolt system showing the GFRP rock bolt, grips, breather holes, and grouting holes.

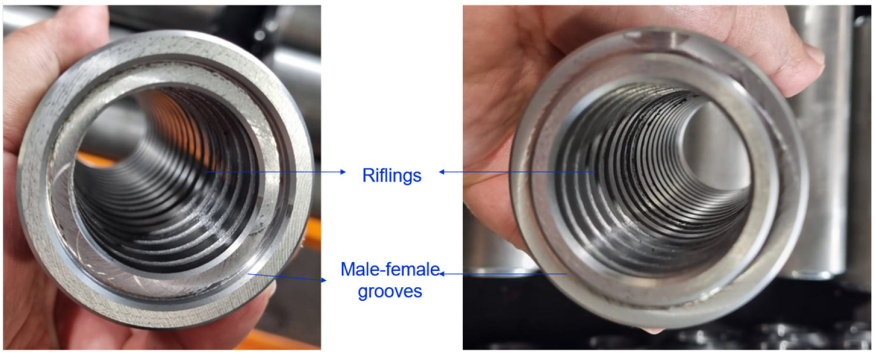
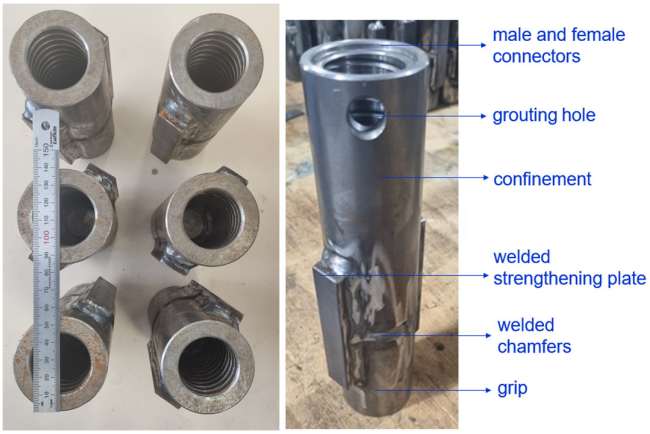


Figure 6. Rifled confinements with interlocking edges.

Once the rock bolts were positioned and the components aligned, the grips were welded to the confinement sections. To prevent weld failure during high-load pull-out testing, two reinforcing plates were welded across each assembly, providing additional structural integrity and ensuring the joints could withstand the applied forces during testing (Figure 7).

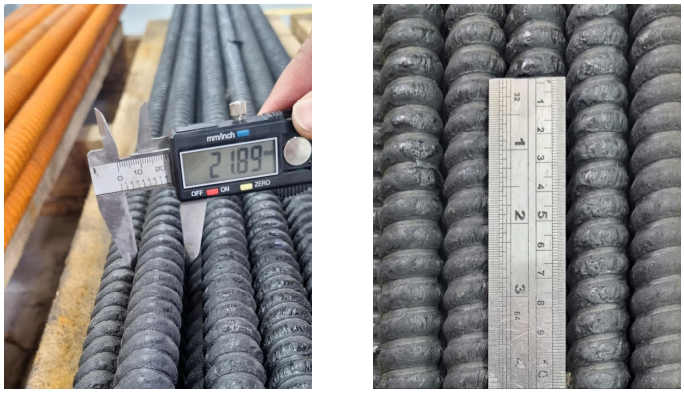


(**a**) (**b**)

Figure 7. Confinement welded to the grip (**a**) top view, (**b**) side view.

2.2.2. Fibreglass Bars

As mentioned earlier, two sizes of GFRP rock bolts, TD22 (22 mm diameter) and TD25 (25 mm diameter), were selected for the experiments. These products were sourced from Jennmar Australia. The specifications of the selected GFRP rock bolts are given in Table 2. The rock bolts were cut to specific lengths based on the embedment configurations and installed within the confinement system. The mechanical properties of the GFRP rock bolts are presented in Table 2, with their physical appearance shown in Figures 8 and 9.



(**a**) (**b**)

Figure 8. 22 mm thrust dowel (**a**) the bolt's diameter, (**b**) the rib distance.



Figure 9. 25 mm thrust dowel (**a**) the bolt's diameter, (**b**) the rib distance.

Table 2. Mechanical characteristics of thrust dowels.

Bolt name	Bolt Diameter (mm)	Cross-Sectional Area (mm²)	Ultimate Tensile Strength (kN)	Elongation (%)	Mass/Meter (kg/m)
TD22	22	340	230	2	0.61
TD25	25	434	300	2	0.95

2.2.3. Bonding Medium

A high-strength, thixotropic grout (TD80), sourced by Jennmar Australia, was used as the bonding agent to ensure full encapsulation of the GFRP rock bolts within the confinement system. The grout was selected due to its excellent pumpability and expansion characteristics, which help eliminate voids and ensure consistent bonding throughout the encapsulation length.

2.3. Casting Procedure

The assembled samples were grouped by ELs, positioned on the laboratory bench, and prepared for grouting. The bonding agent was mixed according to the manufacturer's specifications, with a 35% water-to-grout ratio, and pumped into each sample through the designated grouting ports. Visual confirmation of grout exiting the breather holes ensured complete encapsulation of the rock bolts. The samples were then left to cure according to the testing schedule, with pull-out tests planned for 7, 14, 21, and 28 days of curing. The whole sample preparation process is illustrated in Figure 10.

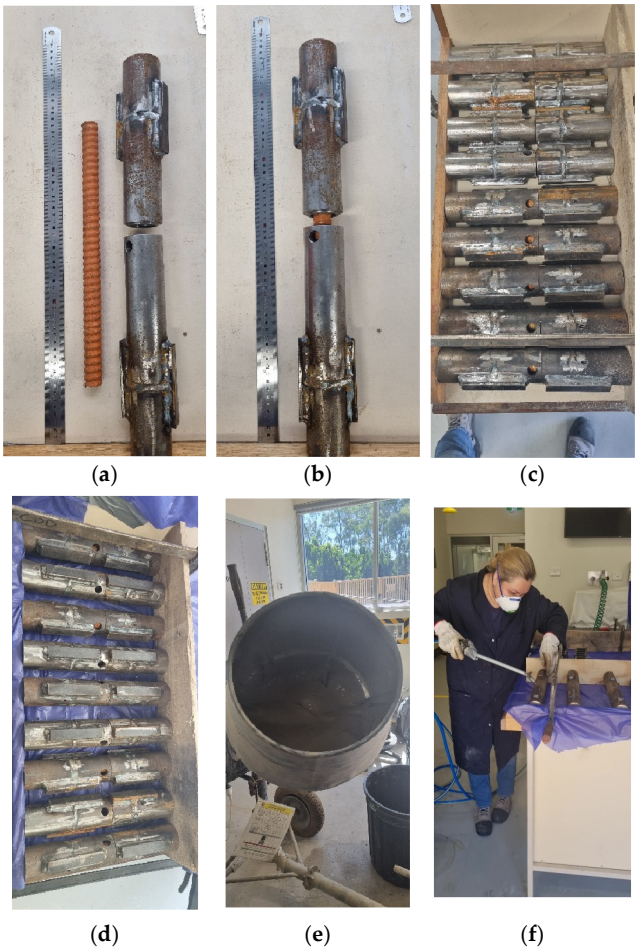


Figure 10. Assembling the samples (**a**, **b**), arranging and fixing the samples (**c**,**d**), mixing the grout (**e**), and pumping the grout (**f**).

2.4. Material Property Tests

2.4.1. Shear Tests

Shear testing is a standard laboratory method used to evaluate the shear strength and deformation characteristics of reinforcement elements, which are essential for assessing their performance in underground support systems [46–48]. In this study, both single-shear and double-shear tests were performed to investigate the shear behaviour of fully grouted GFRP rock bolts. A total of ten samples of both fibreglass rock bolt types, TD22 and TD25, were tested in this study.

Single Shear Tests

In a pure single shear test, the rock bolt element is subjected to shear loading along a single plane by applying force perpendicular to its longitudinal axis using a sharp-edged steel plate. The rock bolt element is fixed in place using a specially designed holder, and the load is increased until shear failure occurs. The shear strength is calculated by dividing the peak load by the cross-sectional area of the fracture surface [49]. Four GFRP rock bolts, each 200 mm in length, were tested using the single shear setup. The shear test setup for this configuration is shown in Figure 11.

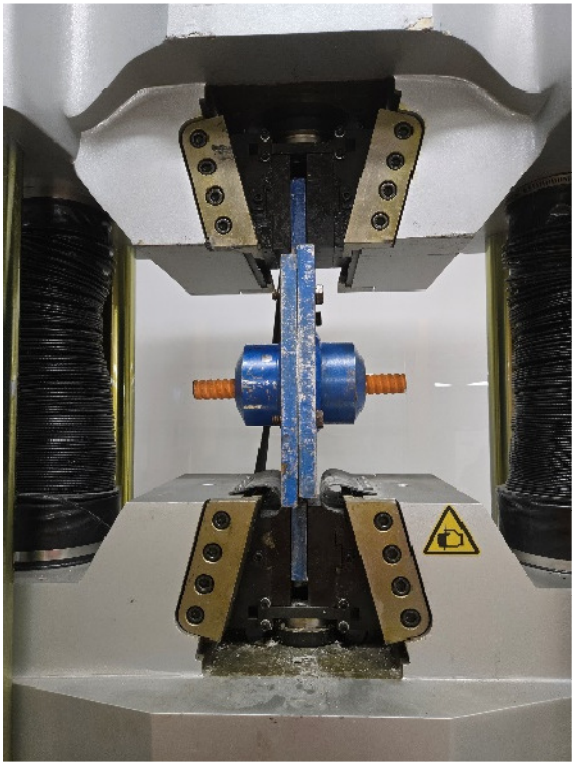


Figure 11. Single shear test.

Double Shear Tests

In the double-shear test, the specimen is positioned within a loading apparatus that simultaneously induces shear along two parallel planes. This configuration provides a more distributed loading environment, allowing for the evaluation of rock bolt behaviour under conditions closer to those encountered in real-world underground installations. In this case, the shear strength is determined by dividing the failure load by twice the cross-sectional area of the rock bolt [49,50]. Six GFRP rock bolts, each 170 mm in length, were

tested using the double shear configuration setup. The shear test setup for the double shear test configurations is shown in Figure 12.

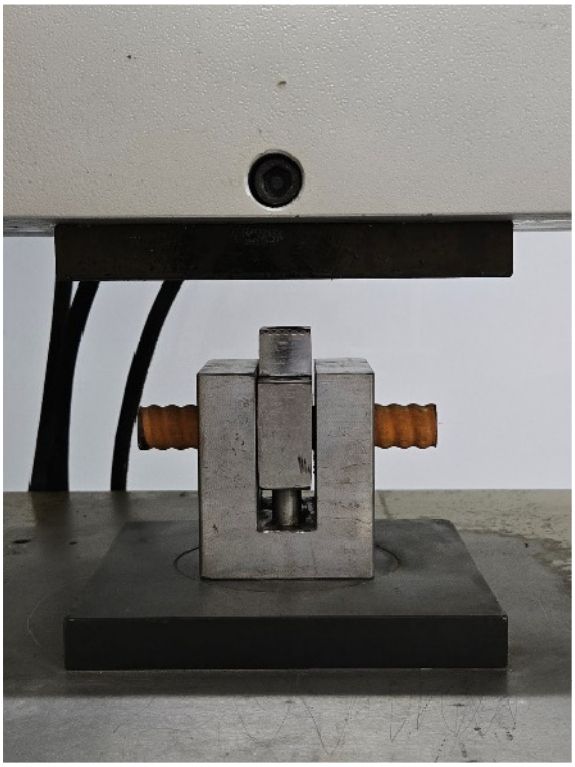


Figure 12. Double shear test.

2.4.2. Uniaxial Compressive Strength Test

To evaluate the mechanical characteristics of the grout used in this study, uniaxial compressive strength (UCS) tests were conducted at various curing stages. Previous studies have highlighted the critical role of grout strength development over time, with factors such as curing duration, water-to-grout ratio, and material composition affecting UCS [51–54]. A total of 12 cubic grout specimens, each measuring 50 × 50 × 50 mm, were prepared from the same grout mixture used in the pull-out tests. The specimens were cast in steel moulds, demolded after 24 h, and cured under controlled laboratory conditions (Figures 13 and 14).

UCS tests were conducted at four curing times: 7, 14, 21, and 28 days, with three specimens tested at each interval. The specimens were loaded using a compression testing machine until failure occurred, and the peak load was recorded. The compressive strength was calculated by dividing the failure load by the cross-sectional area of the specimen.

The results provided essential input for understanding the grout's strength progression over time, which was further incorporated into the numerical simulations to ensure realistic modelling of grout behaviour under axial loading. The post-failure appearance of a grout specimen is shown in Figure 15.

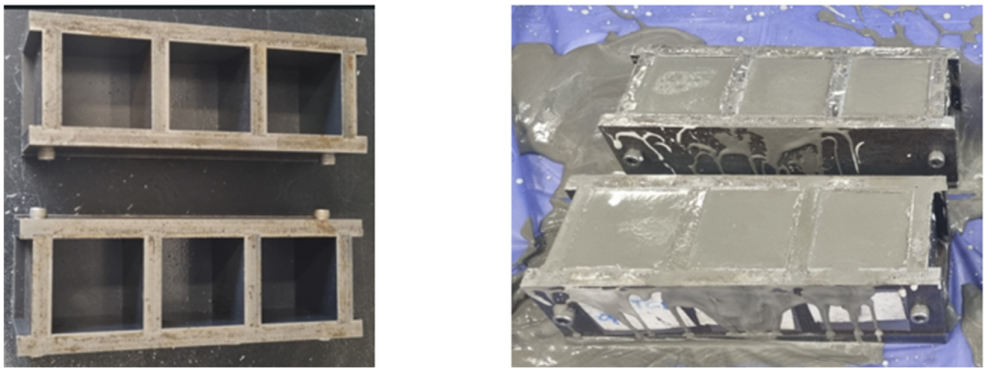


Figure 13. Preparation of grout mixture and casting of cubic specimens for UCS testing (50 × 50 × 50 mm).

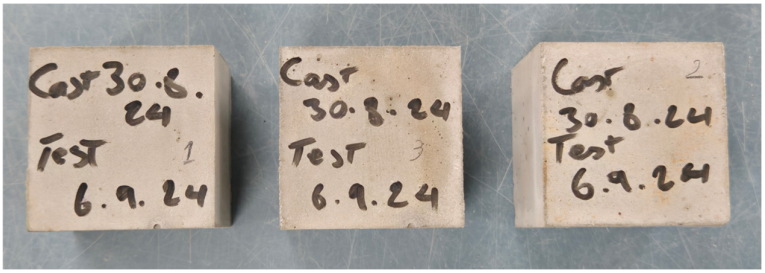


Figure 14. Cured grout specimens before UCS testing.



Figure 15. Grout specimen after UCS failure under uniaxial compressive loading.

2.5. Rock Bolt Mechanical Tests

Pull-Out Tests

Pull-out testing is one of the most widely used techniques to assess the axial load transfer behaviour of rock bolts [17,55–57]. In this study, a comprehensive pull-out test program was conducted to evaluate the performance of fully grouted fibreglass (GFRP) rock bolts under varying embedment lengths, rock bolt diameters, and curing times.

For each rock bolt type, three different ELs were examined to capture the influence of bonded length on axial load capacity: short embedment length of 50 mm, medium length of 100 mm, and long embedment length of 150 mm. To assess the time-dependent bond development, samples were tested at four various curing times: 7, 14, 21, and 28 days, to reflect the progressive development of the mechanical interlock and adhesive bond within the grout-rock bolt system. The whole testing matrix, including rock bolt types, ELs, and curing durations, is previously summarised in Table 1.

To conduct the required pull-out tests, a 1000 kN capacity MTS universal testing machine, located at the University of Southern Queensland, was used. During testing, the prepared samples were subjected to axial displacement at a constant rate of 1 mm/min, simulating the gradual pull-out loading that occurs in the field. The axial load and displacement data were continuously recorded by the machine and transferred to a

connected computer system for processing and analysis. The collected data were used to generate load–displacement curves for each test configuration.

For the first sample, an extensometer was attached to measure the axial elongation of the rock bolts during testing (Figure 16). Special holders were designed to mount the extensometer securely on the sample. A comparison between the MTS machine data and extensometer readings (Figure 17) showed excellent agreement, validating the accuracy of the displacement measurements. For the remaining tests, data from the MTS machine were used exclusively.

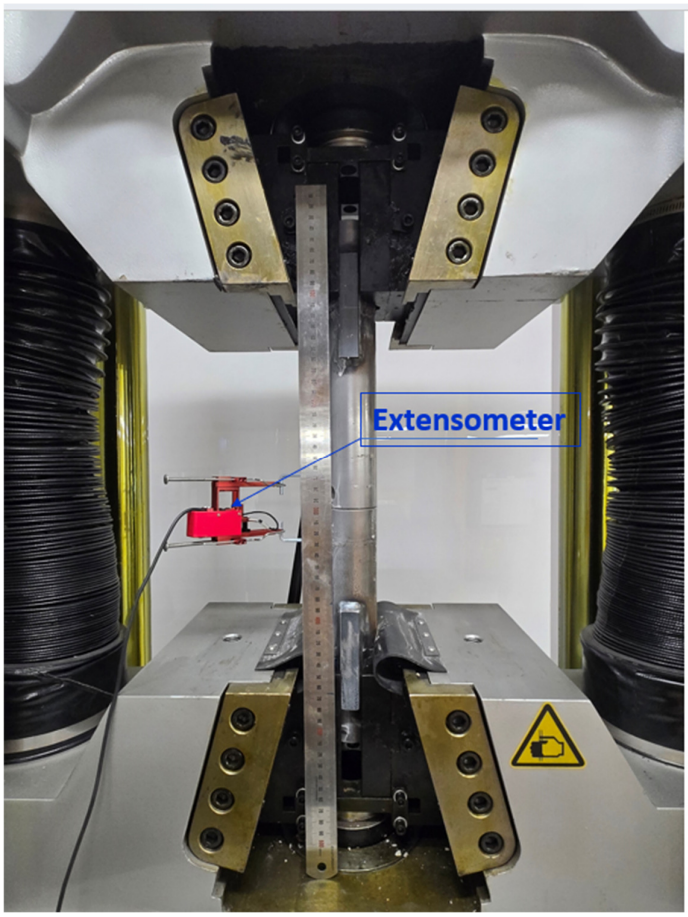


Figure 16. Extensometer attached to the sample.

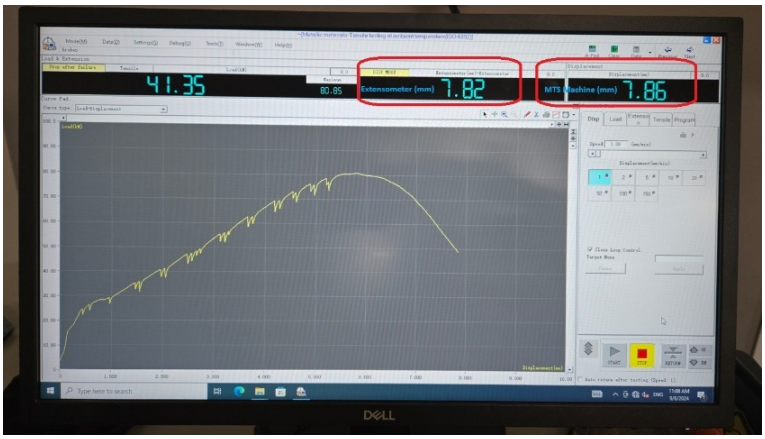


Figure 17. Comparing results from the extensometer and MTS machine.

The results obtained from the experimental program, including shear tests, pull-out tests, and uniaxial compressive strength measurements, provided valuable insights into the mechanical behaviour of fully grouted fibreglass rock bolts. Additionally, numerical simulations were conducted to extend the experimental findings and further investigate the influence of material properties and boundary conditions on the load transfer mechanisms. The detailed findings and interpretations from both the experimental and numerical investigations are presented in the following sections.

3. Results and Discussions

The results of the experimental program are presented in this section, beginning with the shear performance of the GFRP rock bolts, followed by the axial load transfer behaviour from pull-out tests, and concluding with numerical simulation outcomes to complement and expand upon the experimental findings.

3.1. Shear Test Results

As mentioned before, to evaluate the shear behaviour of fibreglass rock bolts, both single-shear and double-shear tests were conducted on TD22 and TD25 rock bolt specimens. The load–displacement responses from the single-shear tests are presented in Figure 18. The TD22 rock bolts demonstrated higher peak loads and greater displacements at failure compared to the TD25 rock bolts, indicating superior shear strength and a more ductile failure mode. The load–displacement curves for TD22 rock bolts showed a gradual increase in load followed by a controlled decline after peak load, characteristic of ductile material behaviour. In contrast, TD25 rock bolts exhibited a steeper initial slope and a sharper load drop post-peak, suggesting more brittle behaviour.

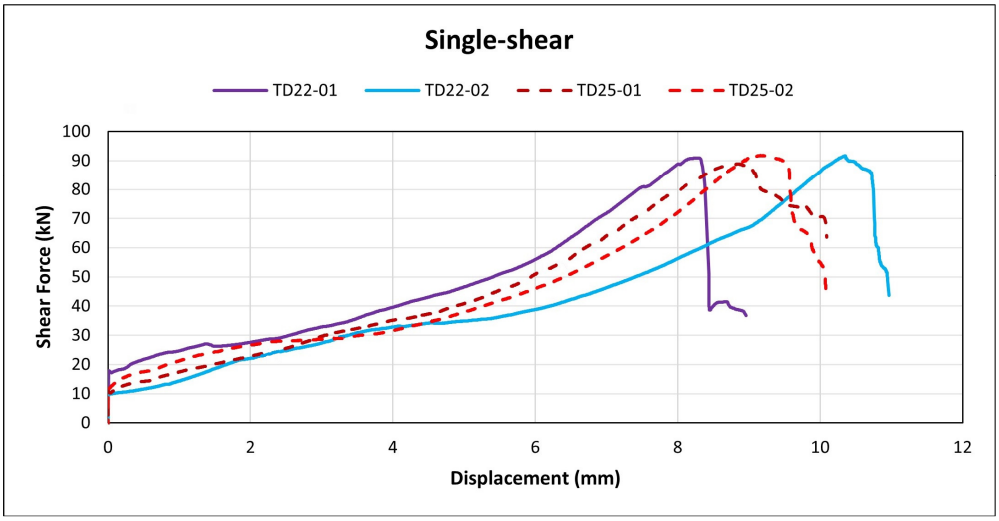


Figure 18. Shear force-displacement graph for single shear tests.

Similar trends were observed in the double-shear tests, as shown in Figure 19. TD22 rock bolts consistently exhibited higher peak loads and larger displacements at failure compared to TD25 rock bolts. The load–displacement curves further confirmed the greater ductility and energy absorption capacity of the TD22 rock bolts, while the TD25 rock bolts displayed more abrupt failure once peak load was reached.

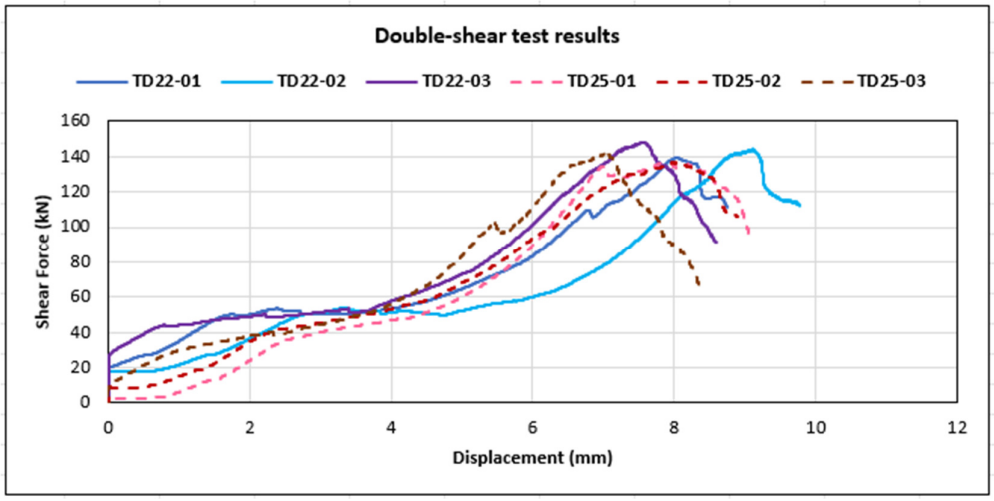


Figure 19. Shear force-displacement graph for double shear tests.

The detailed shear test results, including peak loads and displacements at failure, are summarised in Table 3. Interestingly, the shear test results did not follow the expected trend based on rock bolt diameter. From a mechanical standpoint, a larger diameter should provide a greater cross-sectional area to resist shear. Therefore, the TD25 bolts were anticipated to exhibit higher ultimate shear loads than the TD22 bolts. However, the experimental results showed that the smaller-diameter TD22 bolts achieved comparable or slightly higher peak loads and displayed a more ductile response. This outcome can be attributed to more uniform fibre alignment and resin impregnation within the smaller bolts, reduced stress concentration along the shear planes, and lower stiffness-induced brittleness compared with the TD25 bolts. Moreover, the behaviour of GFRP bolts may differ from that of traditional steel bolts. As reported by Benmokrane et al. [39], the mechanical performance of GFRP rock bolts is highly dependent on the glass content, fibre type, resin system, and manufacturing process, all of which influence the composite's shear and bond characteristics. Hence, while shear capacity in steel rock bolts typically scales directly with diameter, GFRP rock bolts exhibit more complex behaviour governed by internal architecture and material composition.

Table 3. Summary of shear test results for direct and indirect test methods.

Test Type	Specimen	Length (mm)	Peak Load (kN)	Displacement at Peak Load (mm)
Single Shear Test	TD22-01	200	91	8.28
	TD22-02	200	91.7	10.348
	TD25-01	200	88.95	8.835
	TD25-02	200	91.8	9.16
Double Shear Test	TD22-01	170	139.7	8.042
	TD22-02	170	144.3	9.11
	TD22-03	170	148.26	7.597
	TD25-01	170	136	7.799
	TD25-02	170	136.65	7.977
	TD25-03	170	141.8	7.047

Visual inspection of the tested specimens after failure (Figures 20 and 21) supported these observations, with TD22 rock bolts showing more progressive damage and TD25 rock bolts exhibiting sharper fractures.



Figure 20. Fibreglass rock bolts after single-shear test (**Top**: TD25, **Bottom**: TD22).

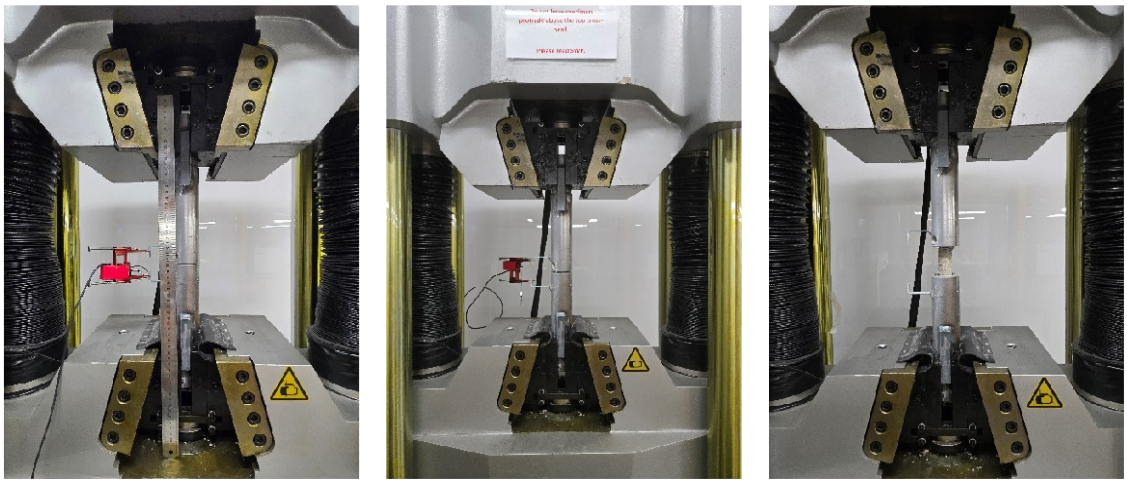


Figure 21. Fibreglass rock bolts after double-shear test (**Top**: TD25, **Bottom**: TD22).

3.2. Pull-Out Test Results

A series of pull-out tests was conducted to assess the axial load transfer behaviour of fully grouted GFRP rock bolts under controlled laboratory conditions. The experimental setup ensured precise alignment of the rock bolts within the steel confinement to simulate practical reinforcement scenarios while minimising eccentricity effects (Figure 22).

Upon completion of the pull-out tests, typical failure patterns were observed at the grout-rock bolt interface. As shown in Figure 23, residual grout adhered to the rock bolt surface after testing, indicating that both mechanical interlock and adhesive bonding contributed to the load transfer mechanism. These observations are consistent with previous research, which highlights the importance of interface bonding and grout deformation in governing the performance of fully grouted rock bolts [7].



(**a**) (**b**) (**c**)

Figure 22. Pull-out test set up (**a**) before, (**b**) during the test, and (**c**) after the test.



(**a**) (**b**)

Figure 23. Sample after the pull-out test (**a**) side view, and (**b**) top view.

The peak axial load results obtained for all test configurations are summarised in Figure 24, illustrating the combined influence of grout curing time, rock bolt diameter, and embedment length on axial performance. As expected, longer curing periods resulted in higher peak loads due to the progressive development of grout strength and improved bond quality. Additionally, rock bolts with larger diameters and longer embedment lengths consistently demonstrated higher load-bearing capacity [23,58], confirming the critical role of both geometric and material factors in optimising reinforcement performance.

At 28 days of curing, the TD25-150 sample achieved a maximum recorded peak load of approximately 116.2 kN, with the TD22-150 rock bolts also exhibiting a high axial capacity of 114.59 kN. These results reinforce the understanding that both grout maturation and bonded length enhance axial performance, while larger rock bolt diameters provide additional surface area for mechanical interlock and adhesive bonding.

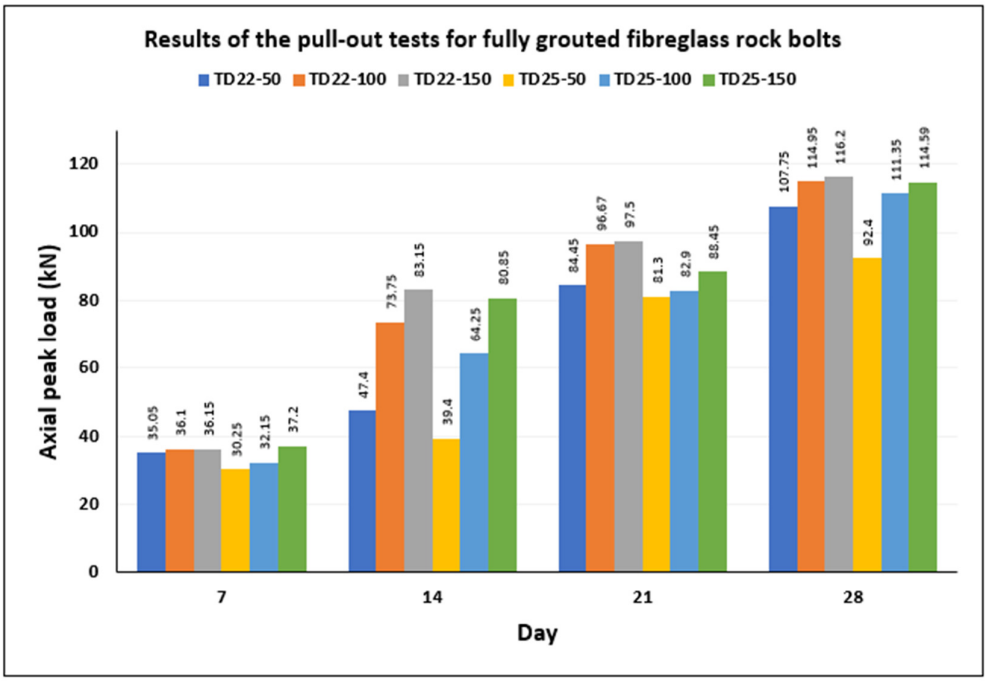


Figure 24. Axial peak load (kN) measured during pull-out tests of fully grouted fibreglass rock bolts with varying rock bolt diameters, embedment lengths, and grout curing times.

The load–displacement responses of TD22 rock bolts after 7 days of curing are presented in Figure 25. All samples exhibited an initial linear phase corresponding to elastic deformation, followed by peak load mobilisation and subsequent bond degradation. Longer ELs resulted in higher peak loads (36.15 kN), whereas shorter lengths were associated with earlier bond failure and reduced capacity (35.05 kN).

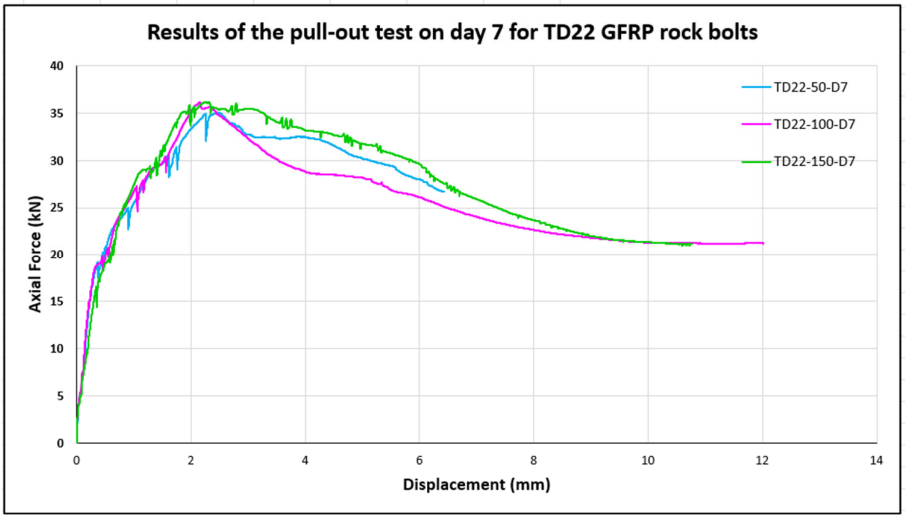


Figure 25. Pull-out test results for TD-22s on day 7.

A similar load–displacement trend was observed for TD25 rock bolts (Figure 26), with these rock bolts demonstrating higher peak loads than the TD22 samples under equivalent curing conditions. The increased capacity of the TD25 rock bolts is attributed to their larger interface area, which promotes greater mechanical interlock and bond

strength. Despite this, both rock bolt types displayed softening behaviour after peak load, highlighting the progressive failure and slip at the grout-rock bolt interface.

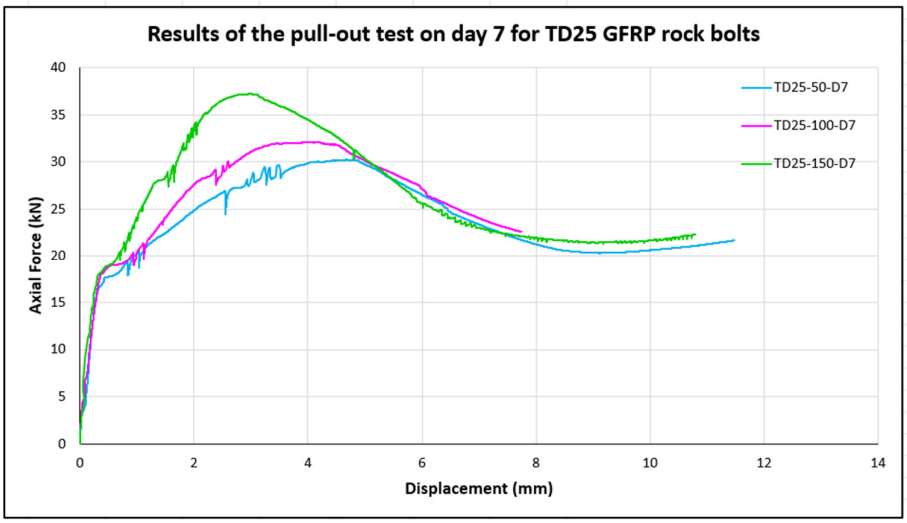


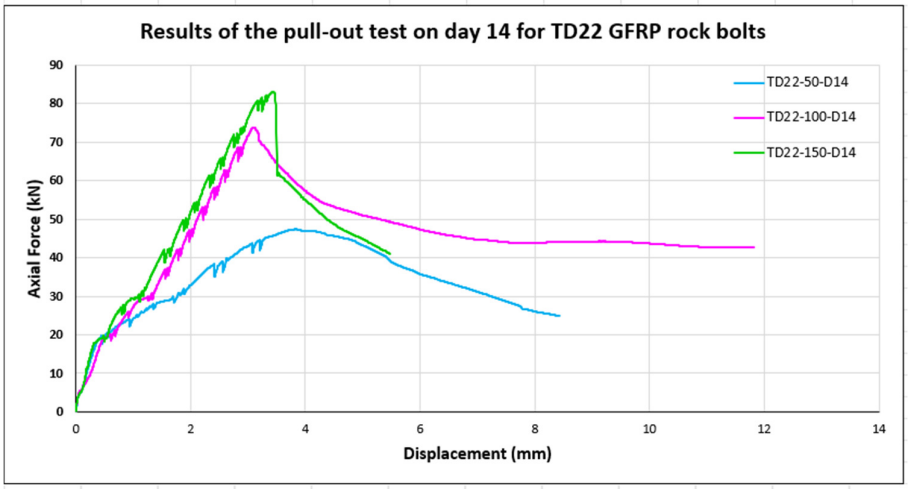
Figure 26. Pull-out test results for TD-25s on day 7.

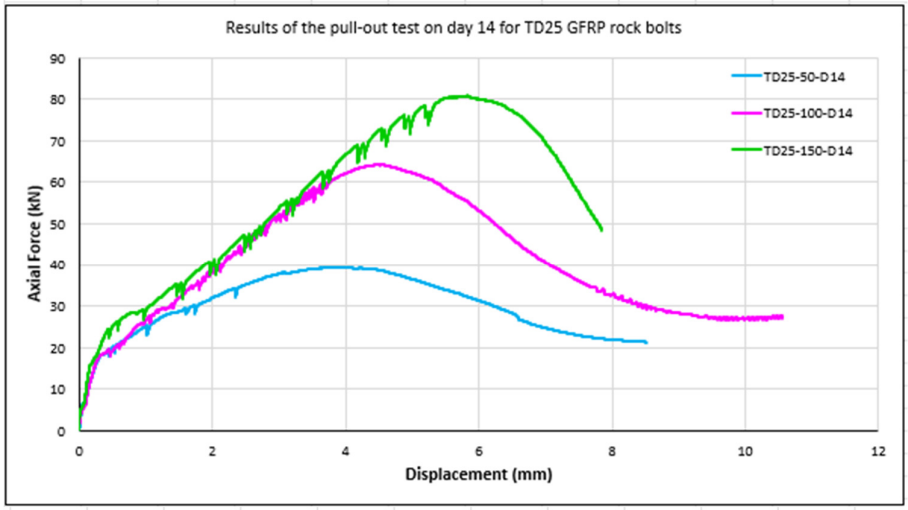
The load–displacement results for the remaining curing times are presented in Figure 27, providing a clear comparison of how axial load transfer performance evolved as the grout strength progressively increased. The influence of ELs on peak load capacity and bond degradation remained evident across all curing stages, with longer embedment lengths consistently improving system performance. At all curing ages, GFRP rock bolts with greater ELs exhibited higher pull-out capacities, confirming that a longer bonded interface enables more effective load transfer between the bolt and the surrounding grout.

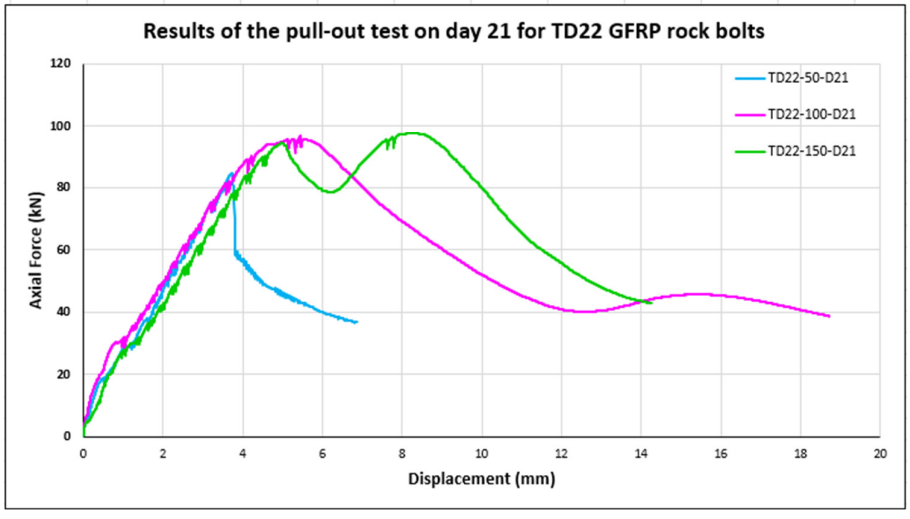
At 7 days, the influence of EL was minor due to incomplete grout hydration; the peak load increased from 35.05 kN (TD22-50) to 36.15 kN (TD22-150), representing an improvement of approximately 3.1%. As curing progressed, the effect became more pronounced. At 14 days, the axial capacity for TD22 increased from 47.4 kN (EL = 50 mm) to 83.15 kN (EL = 150 mm), representing a 75% increase. Similarly, for TD25 bolts, the load increased from 39.4 kN to 80.85 kN, representing a 105% improvement.

As curing advanced to 21 days, the trend continued, though the rate of improvement gradually stabilised. At 21 days, the longer TD22-150 bolts reached 96.67 kN, approximately 14% higher than the shortest embedment, while TD25-150 achieved 88.45 kN, about 9% higher than TD25-50.

By 28 days, when the grout was fully cured, the embedment effect became dominant: the TD22-150 sample reached 116.2 kN, compared with 107.75 kN for TD22-50, indicating an increase of approximately 8%. For TD25 bolts, the capacity increased from 92.4 kN (EL = 50 mm) to 114.59 kN (EL = 150 mm), corresponding to a 24% improvement.


Results of the pull-out test on day 14 for TD22 GFRP rock bolts
Axial Force (kN)
Displacement (mm)
TD22-50-D14
TD22-100-D14
TD22-150-D14


Results of the pull-out test on day 14 for TD25 GFRP rock bolts
Axial Force (kN)
Displacement (mm)
TD25-50-D14
TD25-100-D14
TD25-150-D14


Results of the pull-out test on day 21 for TD22 GFRP rock bolts
Axial Force (kN)
Displacement (mm)
TD22-50-D21
TD22-100-D21
TD22-150-D21

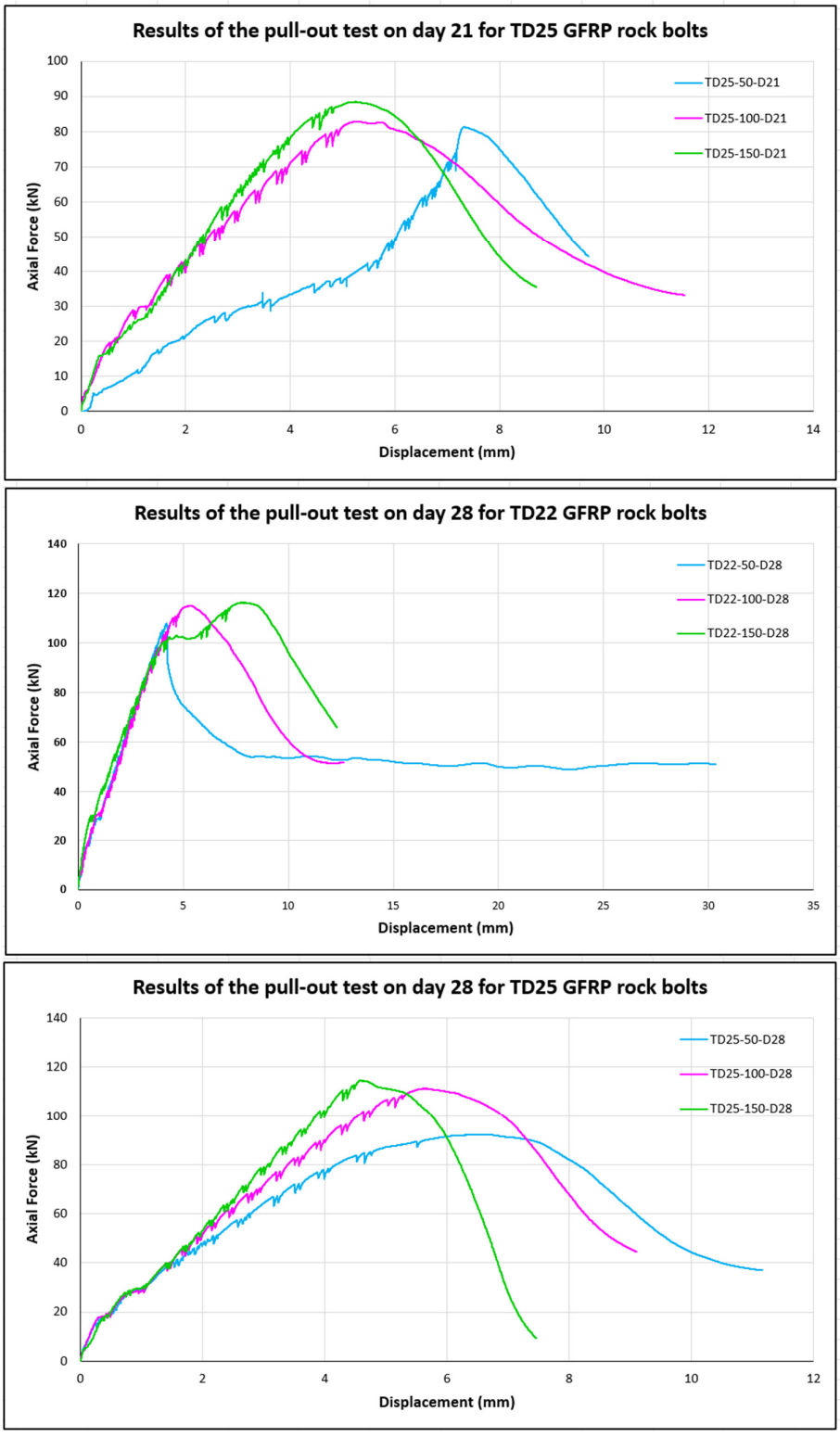


Figure 27. Load–displacement responses of fully grouted GFRP rock bolts tested at 14, 21, and 28 days of curing for different embedment lengths.

The results of the pull-out tests highlighted the importance of grout curing time, EL, and rock bolt diameter in determining load transfer efficiency, while also confirming the contribution of interface bonding mechanisms to this process. These experimental results

formed the foundation for calibrating the subsequent numerical simulations and parametric studies.

3.3. Numerical Simulation

To complement the experimental investigation and provide deeper insight into the axial load transfer mechanisms of fully grouted fibreglass rock bolts, a series of numerical simulations was performed using 3DEC 7.0 (Three-Dimensional Distinct Element Code). 3DEC is a powerful numerical modelling tool developed by Itasca Consulting Group that employs the Distinct Element Method (DEM) to simulate the behaviour of discontinuous and jointed rock masses. The software's ability to model structural elements such as rock bolts, combined with its capability to handle complex boundary conditions and material interactions, makes it particularly suitable for simulating pull-out tests and analysing the load transfer processes along grouted reinforcement systems. In this study, a detailed 3DEC model of the fibreglass rock bolt was developed to replicate the laboratory pull-out tests and assess the influence of grout properties, interface roughness, and boundary conditions on the axial performance of fully grouted fibreglass rock bolts. The model incorporated material properties derived from experimental tests to ensure a realistic simulation of the load–displacement behaviour observed in the laboratory. The numerical modelling framework, model calibration process, and sensitivity analyses are presented in the following sections.

3.3.1. Developing the Fully Grouted Fibreglass Rock Bolt Model

In this study, the GFRP rock bolt was modelled using a pile element, which is designed explicitly in 3DEC to simulate linear structural members such as bolts, anchors, and piles. The pile element consists of a series of interconnected nodes, with coupling springs representing the mechanical interaction between the rock bolt and the surrounding rock mass. These springs enable the transfer of both axial and shear forces, allowing the model to simulate load transfer mechanisms along the grout-rock bolt interface realistically (Figure 28).

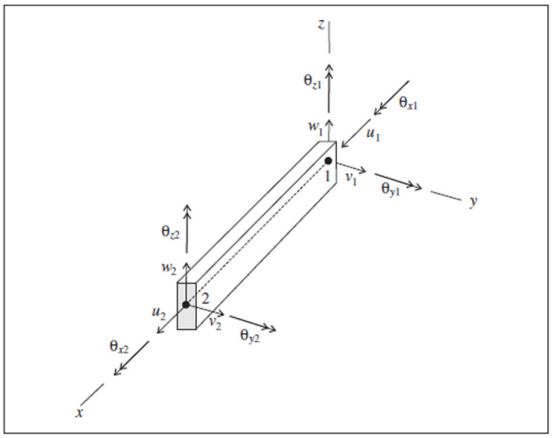


Figure 28. Local coordinate system of a pile element and the degrees of freedom at each endpoint [39].

The interaction between the pile element and the surrounding material is governed by two sets of springs:

- Axial springs, which deform along the bolt's longitudinal axis, capture the transfer of tensile loads.

- Shear springs, which deform perpendicular to the bolt, represent shear interaction and bond behaviour at the interface (Figure 29).

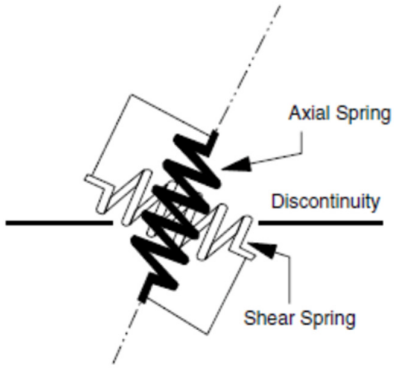


Figure 29. Orientation of coupling springs [39].

The parameters assigned to the interface springs in the numerical model were obtained through a back-calculation process based on the pull-out test results. Initial estimates of the normal and shear stiffness were derived from the theoretical relationships provided in the 3DEC framework, where the spring stiffness depends on the elastic properties and geometry of the bonded materials [59]. These preliminary values were refined iteratively until the simulated load–displacement curves reproduced the experimental results in both stiffness and peak load. Cohesion and bond strength were determined from the measured peak axial loads, while the stiffness values were adjusted to match the initial elastic response and post-peak softening behaviour. The same calibration approach was applied to the rock bolt–grout, grout–grip, and grout–rock interfaces to ensure that the model accurately represented the observed load-transfer mechanisms. The material properties for the rock bolt, grout, and surrounding rock were defined based on experimental testing and literature values. A summary of the key material parameters used in the 3DEC model is provided in Table 4, ensuring that the numerical simulations accurately represent the mechanical behaviour observed in laboratory conditions.

Table 4. Material properties of the fully grouted fibreglass rock bolt used in the 3DEC code.

Category	Parameter Name	Value	Unit	Description
Geometry—Domain	ConL1	0.2	m	Length of first confinement
	ConL2	0.15	m	Length of second confinement
	ConR	0.0275	m	Radius of confinement
	ConRConcrete	0.125	m	Radius of the concrete block
Material—Rock	(assigned directly)	2.9 e10	Pa	Bulk modulus of rock
		1.5 e10	Pa	Shear modulus of rock
		2400	kg/m^3	Density of rock
		10 e6	Pa	Mohr-Coulomb cohesion
		40	degrees	Mohr-Coulomb friction angle
Joint Properties	jkn_	3 e11	Pa/m	Normal stiffness of joints
	jks_	3 e11	Pa/m	Shear stiffness of joints
	jfric_	35	degrees	Friction angle of joints
Pull-Out Loading	xvel_	0.1	m/s	Applied pull-out velocity
Displacement Target	gp_monitor	0.02	m	Monitoring the grid point for a 20 mm displacement limit
Angle Test	dincl_	90	degrees	Inclination of rock bolt (for orientation testing)

Selecting an appropriate constitutive model to represent material behaviour in the simulation is essential for accurately capturing the mechanical response of the system. In this study, an elastic model was applied to simulate the performance of the steel confinements, incorporating their experimentally defined material properties, including Young's modulus, Poisson's ratio, and density. For the surrounding rock mass, the Mohr-Coulomb failure criterion was adopted to represent the rock's strength and deformation behaviour. This widely used model accounts for both cohesion and internal friction, enabling the simulation of rock fracturing, bond degradation, and failure processes [60].

The numerical algorithms in 3DEC continuously track the stress state at contact points between blocks. When the Mohr-Coulomb failure conditions are satisfied, the software adjusts contact forces and displacements to replicate the onset and progression of material failure within the rock mass, providing a realistic representation of ground response under axial loading.

The complete numerical model, including the rock bolt element, confinement structure, and surrounding rock mass, is shown in Figure 30, along with the simulated stress distribution during pull-out loading.

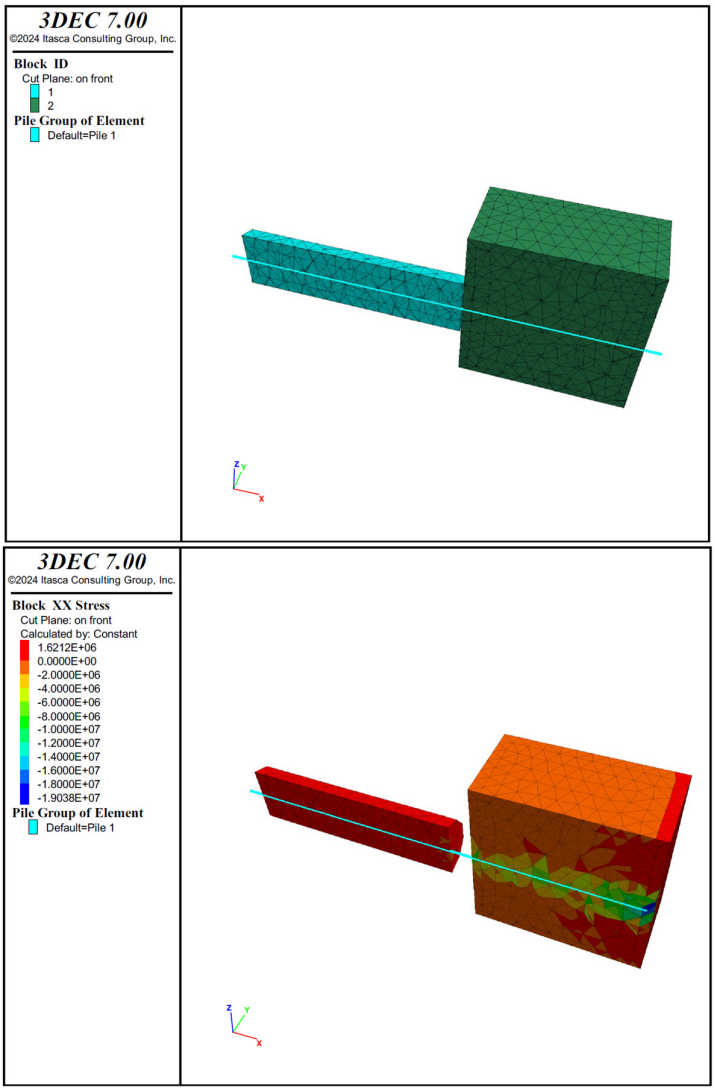


Figure 30. 3DEC model of the fully grouted fibreglass rock bolt system: (**top**) initial model configuration showing the rock bolt and confinement arrangement; (**bottom**) simulated stress distribution within the rock mass during axial pull-out loading.

3.3.2. Model Calibration for Fully Grouted Fibreglass Rock Bolt

To verify the accuracy of the numerical model and ensure a realistic simulation of load transfer behaviour, the 3DEC model was calibrated against experimental pull-out test results. The calibration process focused on comparing key aspects of the load–displacement response, including the initial stiffness, peak load capacity, displacement at peak load, and the post-peak softening trend.

The test configuration selected for model calibration was the TD25-150-D28 rock bolt, which provided precise and reliable experimental data suitable for validating the numerical simulation. A comparison between the numerical and experimental results is presented in Figure 31.

The simulated load–displacement response for the TD25-150-D28 rock bolt was compared with the corresponding experimental results to evaluate the model's performance. As shown in Figure 31, the numerical model successfully reproduced the general behaviour of the experimental load–displacement curve.

In the initial loading phase, both the simulation and experimental results demonstrated a linear relationship between load and displacement, confirming that the elastic properties of the fibreglass rock bolt and the grout-rock bolt interface were appropriately defined in the model. The initial slope, representing system stiffness, was in close agreement with the two datasets, validating the chosen material parameters and interface stiffness.

The peak load predicted by the simulation was slightly lower than that recorded in the laboratory tests, with the numerical model achieving approximately 97% of the experimentally observed peak load. This minor discrepancy falls within acceptable limits, given the inherent simplifications of the numerical model, particularly concerning interface behaviour and grout heterogeneity.

In the post-peak phase, the experimental data showed a sharper load drop after peak mobilisation, indicative of brittle bond failure at the grout-rock bolt interface. The numerical model captured this general softening behaviour, although the simulated load reduction was more gradual. This difference is attributed to the idealised representation of the grout-rock bolt interface in the model, which may not fully account for the complex fracture and debonding processes occurring in the actual grout during failure. Despite these minor deviations, the numerical results closely aligned with the experimental observations, confirming that the developed 3DEC model reliably captures the key mechanical behaviours of fully grouted fibreglass rock bolts under axial pull-out loading.

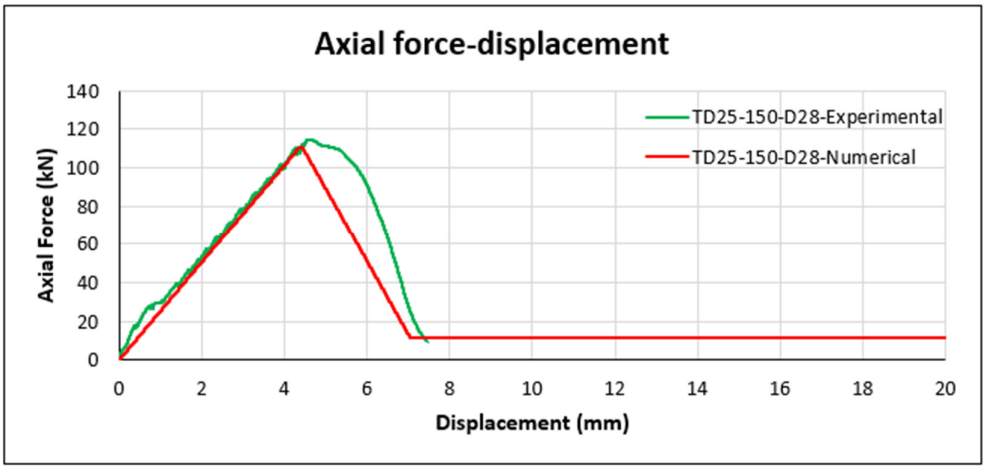


Figure 31. Comparison of experimental and numerical load–displacement curves for TD25-150-D28 fibreglass rock bolt under pull-out loading.

3.3.3. Sensitivity Analysis

Following successful model calibration, a series of numerical sensitivity analyses, including three various scenarios, were performed to investigate further how key parameters influence the axial load transfer behaviour of fully grouted fibreglass rock bolts. These analyses aimed to systematically assess the effects of grout stiffness, interface roughness, and boundary confining stress on load–displacement response and failure characteristics.

By isolating individual parameters within the calibrated 3DEC model, the simulations provided valuable insights into how material properties and installation conditions contribute to the overall performance of the reinforcement system. The results offer practical guidance for optimising rock bolt design, grout selection, and installation practices, particularly in varying underground environments.

Scenario 1: Grout Stiffness

The stiffness of the grout surrounding the rock bolt plays a critical role in governing the axial load transfer capacity of fully grouted reinforcement systems. In this context, grout stiffness refers to the material's ability to resist deformation under applied axial loads, directly influencing how efficiently forces are transferred from the rock bolt into the surrounding rock mass. To quantify the influence of grout stiffness on system performance, a series of numerical pull-out simulations was conducted using the calibrated 3DEC model. Six different grout stiffness values were examined, ranging from 5×10^7 N/m to 5×10^8 N/m, representing variations in grout material quality and field conditions. In all cases, the grout compressive strength was maintained at 40 MPa to isolate the effect of stiffness alone.

The corresponding load–displacement responses for each grout stiffness scenario are presented in Figure 32. As shown in Figure 31, all grout stiffness scenarios produced load–displacement curves with a consistent general shape, characterised by an initial linear-elastic phase, peak load mobilisation, and a post-peak drop in load, eventually stabilising into a residual load phase.

The results indicated that increasing grout stiffness enhances both the initial system stiffness and the peak load capacity. This behaviour reflects the improved ability of stiffer grout to resist higher axial loads compared to less stiff grout types. For instance, the softest grout tested (5×10^7 N/m) exhibited a lower peak load of approximately 45 kN, accompanied by greater displacement before peak mobilisation, indicating reduced load transfer efficiency.

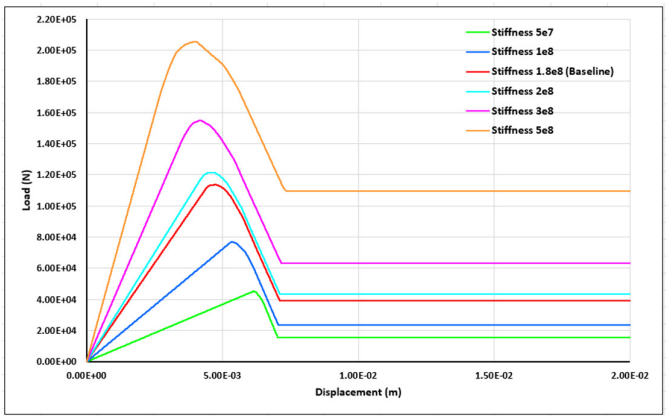


Figure 32. Load–displacement responses of fully grouted fibreglass rock bolts embedded in grout with UCS = 40 MPa, showing different stiffness for the grout.

As grout stiffness increased to 1 × 10^8 N/m and 1.8 × 10^8 N/m, the peak load steadily improved, reaching around 110 kN, which closely matched the experimental grout stiffness value used in the actual experiments. Further increases in grout stiffness to 3 × 10^8 N/m and 5 × 10^8 N/m resulted in even higher peak loads, with the maximum reaching approximately 205 kN for the stiffest grout scenario. However, the stiffer grout configurations also demonstrated a sharper load drop after peak mobilisation, indicating a more brittle system response. In contrast, the softer grout scenarios exhibited a more gradual reduction in load after peak failure, reflecting improved ductility and energy absorption.

These results confirm that while higher grout stiffness improves peak load capacity, it also reduces post-failure stability (i.e., lower peak displacement values), promoting more brittle bond degradation.

Scenario 2: Grout-Rock Bolt Roughness

In addition to grout stiffness, the surface roughness at the grout-rock bolt interface plays a role in controlling load transfer and bond performance in fully grouted rock bolt systems. Rougher interfaces can promote enhanced mechanical interlock and frictional resistance, contributing to higher load capacity and improved post-peak behaviour.

In this study, the roughness was represented indirectly within the 3DEC numerical model by modifying three key interface parameters:

(i) The slip displacement required to mobilise peak shear strength,
(ii) The residual shear strength after peak failure, and
(iii) The interface friction angle.

Together, these parameters control how quickly the interface mobilises peak bond strength, how much load is retained after failure, and the overall ductility of the bond response.

To isolate the effect of interface roughness, five different roughness scenarios (R1 to R5) were defined, as summarised in Table 5, while all other material properties were kept constant, including grout compressive strength at 40 MPa.

Table 5. Grout Roughness Parameter Sets (UCS = 40 MPa fixed).

Case	Slip at Peak (m)	Residual Shear Strength (Pa)	Interface Friction Angle (°)
R1	0.003	0.5 e5	35
R2	0.004	0.8 e5	40
R3	0.005	1.0 e5	45
R4	0.007	1.2 e5	50
R5	0.010	1.5 e5	55

The corresponding load-displacement responses for each grout roughness scenario are presented in Figure 33. As shown, all load-displacement curves exhibited an initial linear phase, corresponding to the elastic deformation of the rock bolt-grout system. The slope of this phase remained consistent across all scenarios, indicating that early stiffness is primarily controlled by the material properties of the rock bolt and grout rather than the interface roughness itself. However, differences emerged after peak load mobilisation. Rougher interfaces, specifically R4 and R5, achieved higher peak loads, 115 kN and 150 kN, respectively, compared to the smoother configurations (R1 to R3). Among the scenarios, R5, representing the roughest interface, attained the maximum peak load of approximately 150 kN, reflecting the enhanced mechanical interlock and shear resistance provided by increased roughness. Conversely, R1, the smoothest interface, demonstrated the lowest peak load, failing to mobilise more than 60 kN before a sharp drop in load

occurred. This indicates a limited bond strength and reduced load transfer efficiency for smoother interfaces. Post-peak behaviour varied between the cases. The smoother scenarios (R1 to R3) experienced abrupt load drops following peak mobilisation, characteristic of brittle bond failure with minimal residual load retention. In contrast, rougher interfaces (R4 and R5) displayed a more gradual reduction in load, eventually stabilising at higher residual load levels. This level has increased from 12 kN in the R1 scenario to 93.5 kN in the R5 scenario, representing an approximately eight-fold increase (679%). This behaviour reflects the increased capacity of rough interfaces to maintain shear resistance after initial bond degradation, primarily due to enhanced frictional contribution and mechanical interlock along the grout-rock bolt interface. These results demonstrate that increasing the roughness of the grout-rock bolt interface improves both peak load capacity and post-failure stability.

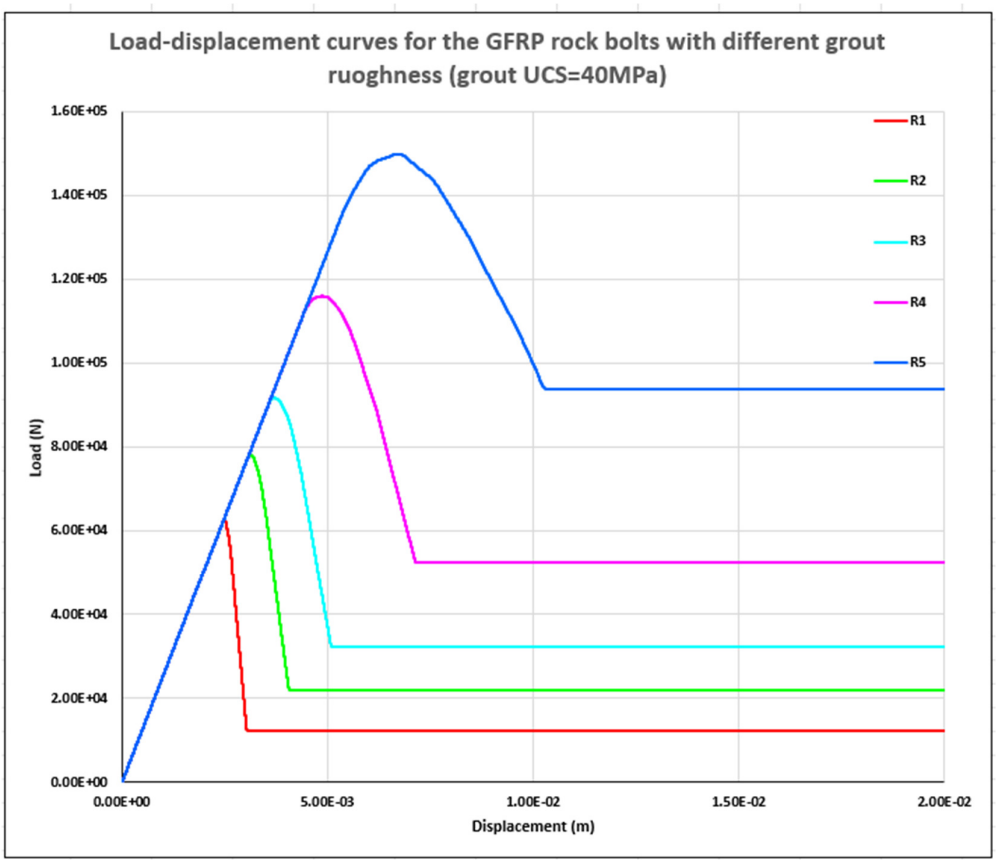


Figure 33. Load–displacement responses of fully grouted fibreglass rock bolts embedded in grout with UCS = 40 MPa, showing the effect of varying interface roughness conditions (R1–R5).

To further assess the influence of interface roughness under different material conditions, an additional set of numerical pull-out simulations was conducted using a reduced grout compressive strength of 20 MPa. The purpose of this scenario was to investigate whether increased interface roughness could still improve bond performance when the surrounding grout is relatively weaker, representing conditions such as early-age installations or sub-optimal grout quality.

As summarised in Table 6, three roughness scenarios (R1 to R3) were defined, representing a progressive increase in interface slip at peak, residual shear strength, and friction angle. All other material properties were kept constant to isolate the effect of roughness.

Table 6. Grout Roughness Parameter Sets (UCS = 20 MPa fixed).

Case	Slip at Peak (m)	Residual Shear Strength (Pa)	Interface Friction Angle (°)
R1	0.002	25,000	35
R2	0.003	40,000	40
R3	0.004	50,000	45

The corresponding load–displacement curves are presented in Figure 34, illustrating the combined impact of reduced grout strength and varying interface roughness on axial load transfer. Despite the lower grout compressive strength, the general trends observed in the previous scenario with 40 MPa grout strength were preserved. All configurations exhibited a consistent initial linear-elastic phase, reflecting elastic deformation of the grout-rock bolt system, followed by peak load mobilisation and subsequent bond degradation. However, the influence of interface roughness became even more pronounced under the reduced grout strength conditions. The smoothest interface (R1) achieved a peak load of only 44 kN, followed by an abrupt drop in load, indicative of brittle debonding and limited post-failure resistance. As interface roughness increased (R2 and R3), both peak load capacity and residual strength improved substantially. Specifically, R2 reached a peak load of approximately 62 kN, while the roughest interface (R3) achieved nearly 78 kN, accompanied by a more gradual decline in load after reaching its peak. The residual load increased from 8.2 kN in R1 to 36 kN in the R3 scenario, reflecting a 34% increase. These results confirm that increasing interface roughness can partially compensate for reduced grout strength, enhancing both peak load capacity and post-peak ductility. The findings highlight the role of interface conditions in determining load transfer performance, particularly in environments where grout quality or curing conditions may be compromised.

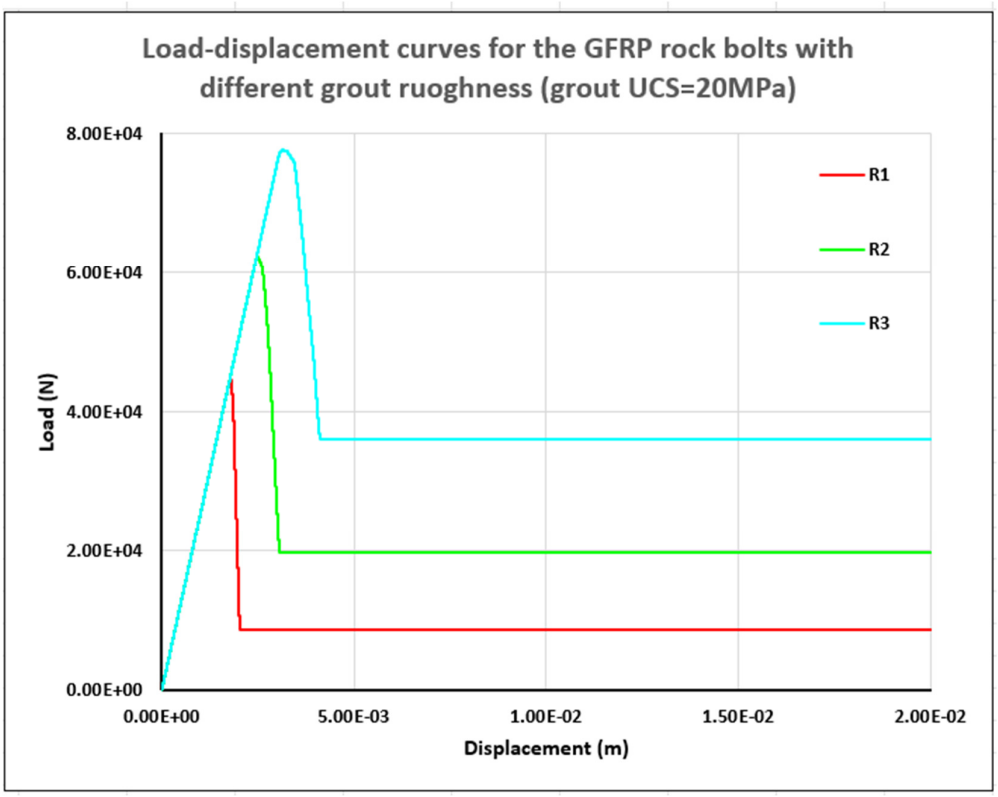


Figure 34. Load–displacement responses of fully grouted fibreglass rock bolts embedded in grout with UCS = 20 MPa, showing the effect of varying interface roughness conditions (R1–R3).

Scenario 3: Confining Stress

In underground environments, the confining stress surrounding the fully grouted rock bolts plays a critical role in governing load transfer performance and failure characteristics. Variations in in situ stress conditions can influence both the axial capacity and post-failure behaviour of reinforcement systems. To investigate these effects, a series of numerical pull-out simulations was performed using the calibrated 3DEC model, focusing on how boundary confinement stresses applied perpendicular to the rock bolt axis affect axial load transfer. The confining stresses were applied in two orthogonal directions:

- σ_{YY}, acting perpendicular to the rock bolt in the Y-direction;
- σ_{ZZ}, acting perpendicular to the rock bolt in the Z-direction;

This approach enabled the systematic assessment of the influence of both isotropic and anisotropic boundary conditions. The following sections present the simulation results for each scenario.

Isotropic Confining Stress

The first set of simulations explored the effect of isotropic boundary conditions, where equal confining stresses were applied in both the YY and ZZ directions. These stresses act perpendicular to the rock bolt axis (X-direction) but in different planes, replicating a uniform, symmetric in situ stress condition often encountered in underground rock masses.

The magnitude of confinement stress was progressively increased from 1 MPa to 5 MPa in both directions across five simulation cases, as summarised in Table 7. All other material and interface properties were kept constant to isolate the influence of boundary stress on load transfer behaviour.

Table 7. Applied isotropic confining stress in ZZ and YY directions for each numerical simulation case.

Case	σ_{ZZ}	σ_{YY}
Iso1	1	1
Iso2	2	2
Iso3	3	3
Iso4	4	4
Iso5	5	5

The resulting load–displacement responses for each confining scenario are presented in Figure 35, providing insight into how isotropic confinement stress affects axial capacity, post-peak performance, and system ductility.

As shown in Figure 35, all simulated scenarios followed a similar load–displacement trend, characterised by an initial linear-elastic phase, peak load mobilisation, and a post-peak reduction in load associated with bond degradation along the grout-rock bolt interface.

While the peak load remained relatively consistent across all confining stress levels, averaging around 110 kN, the post-peak behaviour of the system was influenced by the applied boundary stress. At the lowest confinement stress (Iso1), the load decrease after peak was more gradual, with the system retaining a residual load of approximately 37.5 kN, reflecting a more ductile response and the ability to maintain some load after bond degradation began.

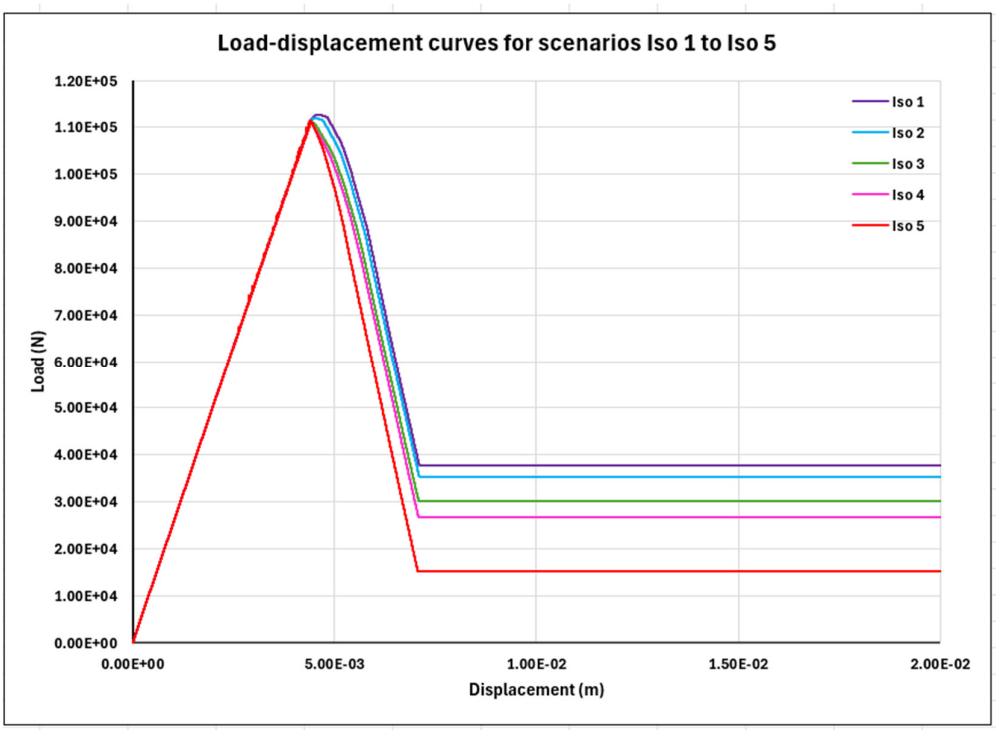


Figure 35. Load–displacement response of fully grouted fibreglass rock bolts under varying isotropic confining stress in numerical simulations.

In contrast, at the highest confinement stress (Iso5), the system exhibited a sharper post-peak load drop, stabilising at a residual load of around 15 kN. The steeper slope in the load–displacement curve reflects a more brittle system response under higher confining stress, where failure occurs more abruptly once peak bond strength is mobilised.

These results indicate that increased boundary confining stress enhances the initial stiffness of the system and enables full mobilisation of the peak load. However, it also restricts deformation around the grout-rock bolt interface, leading to a faster, more brittle loss of load-carrying capacity after failure initiates.

It is essential to note that the applied boundary stresses alone influenced these trends, as all material properties and grout-rock bolt interface conditions were held constant throughout the simulations.

Anisotropic Confining Stress:

In the second set of simulations, anisotropic boundary conditions were applied to evaluate how uneven stress conditions affect axial load transfer in fully grouted fibreglass rock bolts. In these simulations, the rock bolt was oriented along the X-direction, with confining stresses applied perpendicular to the rock bolt axis in both the YY and ZZ directions, but with unequal magnitudes.

For this scenario, the lateral confining stress in the Y-direction (σ_{YY}) was kept constant at 1 MPa, while the confining stress in the Z-direction (σ_{ZZ}) was progressively increased from 1 MPa to 5 MPa, as shown in Table 8. This loading condition represents realistic underground environments where in situ stresses acting perpendicular to reinforcement elements may not be uniformly distributed.

Table 8. Applied anisotropic confining stress in ZZ and YY directions for each numerical simulation case.

Case	σ_{ZZ}	σ_{YY}
Aniso1	1	1
Aniso2	2	1
Aniso3	3	1
Aniso4	4	1
Aniso5	5	1

The corresponding load–displacement curves for each simulation case are presented in Figure 36, illustrating how varying stress in the Z-direction, with constant lateral confining stress, influences load transfer performance.

The results show that increasing σ_{ZZ}, while holding σ_{YY} constant, produced noticeable changes in the post-peak behaviour of the system. The peak load remained relatively stable at approximately 110 kN across all anisotropic confinement levels, indicating that variations in σ_{ZZ} alone do not affect the maximum load-carrying capacity of the system. However, the residual load retained after peak failure progressively decreased as σ_{ZZ} increased. At the lowest confining condition (Aniso1, with $\sigma_{ZZ} = \sigma_{YY} = 1$ MPa), the system retained a residual load of approximately 37.5 kN, reflecting moderate bond degradation but continued load transfer after peak mobilisation. As σ_{ZZ} increased to 5 MPa in Aniso5, the residual load decreased to around 26 kN, and the slope of the post-peak load drop became steeper, reflecting a more brittle system response.

These results demonstrate that increasing confining stress in the Z-direction influences the failure load transfer mechanisms of the grouted reinforcement system (i.e., bond strength), promoting a more abrupt reduction in load-carrying capacity after the peak load is reached. Throughout these simulations, the properties of the grout, rock bolt, and interface materials remained constant, ensuring that the applied confining stress was the sole driver of the observed changes in system response.

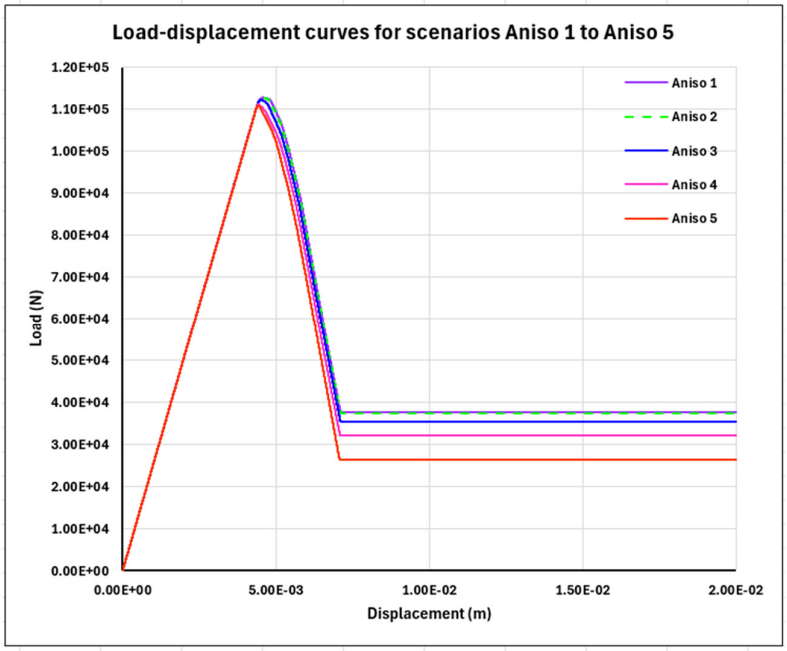


Figure 36. Load–displacement response of fully grouted fibreglass rock bolts under varying anisotropic confining stress in numerical simulations.

The numerical results demonstrate that the boundary confining stress, applied perpendicular to the rock bolt axis, in both the YY and ZZ directions, affects the post-peak behaviour of fully grouted fibreglass rock bolts. Increasing the stress in either direction reduced the residual load retained after bond degradation. It produced a steeper post-peak slope in the load–displacement curves, indicating a shift toward more brittle failure. Although the peak load remained unaffected by the level of confining stress, approximately 110 kN in all scenarios, the system's ability to sustain load beyond peak conditions was influenced by the magnitude and direction of the applied boundary stresses. The residual load decreased about 29.9% in the anisotropic scenario and 59.6% in the isotropic scenario.

4. Conclusions

This study investigated the axial load-transfer behaviour of fully grouted GFRP rock bolts through an integrated experimental-numerical approach, combining pull-out tests with 3DEC simulations. The principal findings are summarised below:

- Single and double-shear behaviour: The results revealed that TD-22 rock bolts achieved higher shear capacity (up to approximately 92 kN in single shear and 148 kN in double shear) and exhibited a more gradual post-peak softening response than the TD-25 bolts (up to approximately 92 kN in single shear and 142 kN in double shear), indicating improved ductility and energy absorption. The smaller-diameter TD-22 bolts also exhibited smoother fracture surfaces and more progressive damage evolution, suggesting a more uniform fibre alignment and lower stress concentrations within the shear zone, likely due to differences in manufacturing quality and material composition.
- Axial response and calibration. Pull-out tests revealed a distinct linear elastic stage, followed by a peak and post-peak softening stage due to interface debonding and slip. The calibrated 3DEC model (pile/rock bolt element) accurately captured this behaviour, reproducing approximately 97% of the experimental peak load, thereby validating its suitability for parametric analyses [45].
- Increasing the ELs from 50 mm to 150 mm resulted in a substantial rise in axial peak load for both GFRP rock bolt types, with TD22 increasing from 47.4 kN to 83.15 kN and TD25 from 39.4 kN to 80.85 kN at 14 days of curing—equivalent to gains of 75% and 105%, respectively. At 28 days, when grout strength was fully cured, the effect of EL remained evident, with TD25-150 and TD22-150 achieving peak loads of 114.59 kN and 116.2 kN, representing improvements of up to 25% over the shortest embedments. These results confirmed that both EL and curing time play decisive roles in enhancing bond mobilisation and overall axial performance of fully grouted GFRP rock bolts.
- Influence of grout stiffness. Increasing grout stiffness elevated the peak load yet resulted in a sharper post-peak decline and lower residual load, reflecting a more brittle load-transfer mechanism. This agrees with previous finite discrete coupling studies on interface damage localisation [27].
- Confining stress conditions. Both isotropic and anisotropic confining stress increased initial stiffness but reduced ductility. The residual load decreased by approximately 59.6% under the highest isotropic confinement and by 29.9% under the highest anisotropic confinement.

5. Prospects and Future Work

Building on the present findings, future research will pursue the following directions:

- Extended confinement mapping: Conduct a broader range of axial loading tests on various GFRP rock bolt types and sizes to develop EL design maps and identify the optimum embedment length for different GFRP rock bolting systems.
- Cyclic and rate-dependent loading. Assess the dynamic response of GFRP rock bolts to cyclical or rapid loading, replicating seismic and blasting conditions.
- Surface geometry optimisation. Investigate parametric effects of rib height, spacing, and angle to refine the GFRP rock bolt's surface design using DEM/FDM simulations.
- In the present study, roughness effects were represented indirectly through equivalent cohesion and stiffness values back-calculated from pull-out tests. This approach captures the combined influence of surface texture, adhesion, and micro-interlocking without requiring direct measurement. Future work should include the direct characterisation of the bolt–grout and grout–rock interfaces. Measured roughness indices could then be incorporated into numerical models to link surface morphology with bond strength.
- Further studies are also recommended using the Finite Element Method (FEM) (e.g., ABAQUS, ANSYS) to complement the DEM analysis. FEM can provide detailed stress and deformation fields within the grout and bolt, allowing a more complete evaluation of how interface geometry and material behaviour interact during load transfer.
- Combining direct roughness measurements with FEM modelling would enhance the predictive accuracy of interface behaviour in fully grouted GFRP bolt systems.

Author Contributions: Conceptualisation, S.E. and A.M.; methodology, S.E. and A.M.; software, S.E. and A.M.; validation, S.E. and A.M.; formal analysis, S.E. and A.M.; investigation, S.E. and A.M., B.J.S., H.N., P.C., K.M., W.K., N.A. and A.E.; resources, S.E., A.M., K.M., W.K. and P.C.; data curation, S.E., A.M. and P.C.; writing—original draft preparation, S.E., A.M. and B.J.S. Writing—review and editing, S.E., A.M., B.J.S., K.M., W.K., N.A., P.C., H.N. and A.E.; visualisation, S.E. and A.M.; supervision, A.M., K.M., W.K. and N.A. All authors have read and agreed to the published version of the manuscript.

Funding: This research received no external funding.

Informed Consent Statement: Informed consent was obtained from all subjects involved in the study.

Data Availability Statement: The data supporting the findings of this study are available upon request from the corresponding author.

Acknowledgments: The authors would like to acknowledge the in-kind support of Jennmar Australia for this research study.

Conflicts of Interest: The authors declare no conflicts of interest. Also, Peter Craig, was employed by the company Jennmar Australia. The remaining author declares that the research was conducted in the absence of any commercial or financial relationships that could be construed as a potential conflict of interest.

References

1. Jodeiri Shokri, B. *A Step Toward Better Understanding Rock Bolt Technology, in School of Engineering*; University of Southern Queensland: Springfield, Australia, 2025; p. 222.
2. Jodeiri Shokri, B.; Mirzaghorbanali, A.; Nourizadeh, H.; McDougall, K.; Karunasena, W.; Aziz, N.; Entezam, S.; Entezam, A. Axial Load Transfer Mechanism in Fully Grouted Rock Bolting System: A Systematic Review. *Appl. Sci.* **2024**, *14*, 5232.

3. Ma, S. *Load Transfer Mechanism of Fully Encapsulated Rockbolts*, *in School of Civil, Mining, and Environmental Engineering*; University of Wollongong: Wollongong, Australia, 2014; p. 264.
4. Thompson, A.G.; Villaescusa, E.; Windsor, C.R. Ground Support Terminology and Classification: An Update. *Geotech. Geol. Eng.* **2012**, *30*, 553–580.
5. Kim, H.; Rehman, H.; Ali, W.; Naji, A.M.; Kim, J.-J.; Kim, J.; Yoo, H. Classification of Factors Affecting the Performance of Fully Grouted Rock Bolts with Empirical Classification Systems. *Appl. Sci.* **2019**, *9*, 4781.
6. Farmer, I.W. Stress distribution along a resin grouted rock anchor. *Int. J. Rock Mech. Min. Sci. Geomech. Abstr.* **1975**, *12*, 347–351.
7. Li, C.; Stillborg, B. Analytical models for rock bolts. *Int. J. Rock Mech. Min. Sci.* **1999**, *36*, 1013–1029.
8. Thenevin, I.; Blanco-Martín, L.; Hadj-Hassen, F.; Schleifer, J.; Lubosik, Z.; Wrana, A. Laboratory pull-out tests on fully grouted rock bolts and cable bolts: Results and lessons learned. *J. Rock Mech. Geotech. Eng.* **2017**, *9*, 843–855.
9. Aziz, N.; Webb, B. Study of Load Transfer Capacity of Bolts Using Short Encapsulation Push Test. In *Proceedings of the 2003 Coal Operators' Conference, Mining Engineering*; University of Wollongong: Wollongong, Australia, 2003; pp. 72–80.
10. Bobet, A.; Einstein, H.H. Tunnel reinforcement with rockbolts. *Tunn. Undergr. Space Technol.* **2011**, *26*, 100–123.
11. Gregor, P. Shear Behaviour of Fibreglass Rock Bolts for Ground Reinforcement, in School of Engineering. Ph.D. Thesis, University of Southern Queensland, Springfield, Australia, 2022.
12. Cao, C.; Jan, N.; Ren, T.; Naj, A. A study of rock bolting failure modes. *Int. J. Min. Sci. Technol.* **2013**, *23*, 79–88.
13. Li, C.C. Principles of rockbolting design. *J. Rock Mech. Geotech. Eng.* **2017**, *9*, 396–414.
14. Cui, G.; Zhang, C.; Pan, Y.; Deng, L.; Zhou, H. Laboratory investigation into effect of bolt profiles on shear behaviors of bolt-grout interface under constant normal stiffness (CNS) conditions. *J. Rock Mech. Geotech. Eng.* **2020**, *12*, 1234–1248.
15. Shi, H.; Song, L.; Zhang, H.; Chen, W.; Lin, H.; Li, D.; Wang, G.; Zhao, H. Experimental and numerical studies on progressive debonding of grouted rock bolts. *Int. J. Min. Sci. Technol.* **2022**, *32*, 63–74.
16. Guan, K.; Jiang, X.; Zhu, W.; Luo, W.; Li, H.; Li, B. Micromechanical model for simulating load transfer behavior and damage evolution for fully grouted rockbolt under axial loads. *Int. J. Rock Mech. Min. Sci.* **2025**, *185*, 105971.
17. Li, Y.; Tan, Y.; Ahmed, A.; Cheng, H. Experimental study on the pullout behaviour of rockbolts with steel fiber-reinforced grout under constant confining pressures. *Constr. Build. Mater.* **2023**, *397*, 132350.
18. Zhang, C.; Cui, G.; Chen, X.; Zhou, H.; Deng, L. Effects of bolt profile and grout mixture on shearing behaviors of bolt-grout interface. *J. Rock Mech. Geotech. Eng.* **2020**, *12*, 242–255.
19. Wang, C.; Jiang, Y.; Wang, G.; Luan, H.; Zhang, Y.; Zhang, S. Experimental investigation on the shear behavior of the bolt-grout interface under CNL and CNS conditions considering realistic bolt profiles. *Geomech. Geophys. Geo-Energy Geo-Resour.* **2022**, *8*, 111.
20. Zhang, Z.; Liu, J.; Luan, H.; Wang, Y.; Jiang, Y.; Shi, Q.; Wang, C.; Zhang, S. Shear Mechanical Properties of Bolt-Grout Interface under Different Bolt Surface Profiles. *Appl. Sci.* **2024**, *14*, 1770.
21. Zhang, S.; Jiang, Y.; Chen, H.; Luan, H.; Zhang, J.; Shang, D.; Zheng, H. Bolt profile and grout strength influence on shear characteristics of the bolt–grout interface. *Phys. Fluids* **2025**, *37*, 043353.
22. Høien, A.H.; Li, C.C.; Zhang, N. Pull-out and Critical Embedment Length of Grouted Rebar Rock Bolts-Mechanisms When Approaching and Reaching the Ultimate Load. *Rock Mech. Rock Eng.* **2021**, *54*, 1431–1447.
23. Li, C.; Kristjansson, G.; Høien, A. Critical embedment length and bond strength of fully encapsulated rebar rockbolts. *Tunn. Undergr. Space Technol.* **2016**, *59*, 16–23.
24. Yu, S.; Zhu, W.; Niu, L. Experimental and numerical evaluation on debonding of fully grouted rockbolt under pull-out loading. *Int. J. Coal Sci. Technol.* **2022**, *9*, 8.
25. Kang, H.; Li, W.; Gao, F.; Yang, J. Grouting theories and technologies for the reinforcement of fractured rocks surrounding deep roadways. *Deep Undergr. Sci. Eng.* **2022**, *2*, 2–19.
26. Hu, Y.; Zheng, M.; Feng, W.; Tong, J.; Wang, Y.; Wang, Q.; Liu, K.; Ye, L. Interface bond degradation and damage characteristics of full-length grouted rock bolt in tunnels with high temperature. *J. Rock Mech. Geotech. Eng.* **2023**, *15*, 2639–2657.
27. Zhang, S.; Luan, H.; Jiang, Y.; Wang, Y.; Li, B.; Liu, Z.; Jiang, T.; Li, X. Study on the Load Transfer and Damage Evolution Characteristics of the Bolt-Grout Interface concerning Bolt Rib Parameters: Based on a Finite-Discrete Numerical Method. *Comput. Geotech.* **2025**, *179*, 107010.
28. Thirukumaran, S.; Oliveira, D.; Ariza, L. Assessing the Relative Quality of Rock Bolt Grouting in Weak Rock Mass Based on In Situ and Numerical Pull-Out Tests. *Rock Mech. Rock Eng.* **2025**, *58*, 10497–10522.
29. Wu, S.; Cao, X.; Zhu, Y.; Skrzypkowski, K.; Zagorski, K. Examination of Stress Corrosion Cracking of Rock Bolts in Simulated Underground Environments. *Materials* **2025**, *18*, 1275.

30. Gregor, P.; Mirzaghorbanali, A.; McDougall, K.; Aziz, N.; Jodeiri Shokri, B. Shear Behaviour of Fibreglass Rock Bolts for Various Pretension Loads. *Rock Mech. Rock Eng.* **2023**, *56*, 8083–8113.
31. Nourizadeh, H. *Axial Load Transfer Mechanism of Rock Bolts*; University of Southern Queensland: Springfield, Australia, 2024; p. 227.
32. Bédard, C. Composite Reinforcing Bars: Assessing Their Use in Construction. *Concr. Int.* **1992**, *14*, 55–59.
33. Aziz, N.; Craig, P.; Nemcik, J.; FI, H. Rock bolt corrosion-an experimental study. In *Proceedings of the Coal Operators' Conference*; University of Wollongong: Wollongong, Australia, 2013; pp. 144–151.
34. Li, H.; Fu, J.; Chen, B.; Zhang, X.; Zhang, Z.; Lang, L. Mechanical Properties of GFRP Bolts and Its Application in Tunnel Face Reinforcement. *Materials* **2023**, *16*, 2193.
35. Nkurunziza, G.; Debaiky, A.; Cousin, P.; Benmokrane, B. Durability of GFRP bars: A critical review of the literature. *Prog. Struct. Eng. Mater.* **2005**, *7*, 194–209.
36. GangaRao, H.V.S.; Taly, N.; Vijay, P.V. *Reinforced Concrete Design with FRP Composites*; CRC Press: Boca Raton, FL, USA, 2006; p. 400.
37. Thomas, A.H. Glass Fibre Reinforced Plastic (GFRP) permanent rockbolts. In *Tunnels and Underground Cities: Engineering and Innovation Meet Archaeology, Architecture and Art*; CRC Press: Boca Raton, FL, USA, 2019; pp. 3200–3209.
38. Phillips, M.G. Prediction of long-term stress-rupture life for glass fibre-reinforced polyester composites in air and in aqueous environments. *Composites* **1983**, *14*, 270–275.
39. Benmokrane, B.; Xu, H.; Bellavance, E. Bond strength of cement grouted glass fibre reinforced plastic (GFRP) anchor bolts. *Int. J. Rock Mech. Min. Sci.* **1996**, *33*, 455–465.
40. Chen, X.; Zhang, D.; Sun, Z.; Chen, W. Extrusion prediction of tunnel face reinforced with fiberglass bolts considering interface debonding. *Phys. Fluids* **2025**, *37*, 036611.
41. Al Omar, S.; Abdelhadi, A. Comparative Life-Cycle Assessment of Steel and GFRP Rebars for Procurement Sustainability in the Construction Industry. *Sustainability* **2024**, *16*, 3899.
42. Sbahieh, S.; Tahir, F.; Al-Ghamdi, S.G. Environmental and mechanical performance of different fiber reinforced polymers in beams. *Mater. Today Proc.* **2022**, *62*, 3548–3552.
43. Gregor, P.; Mirzaghorbanali, A.; McDougall, K.; Aziz, N.; Jodeiri Shokri, B. Investigating shear behaviour of fibreglass rock bolts reinforcing infilled discontinuities for various pretension loads. *Can. Geotech. J.* **2024**, *61*, 414–446.
44. Gregor, P.; Mirzaghorbanali, A.; McDougall, K.; Aziz, N.; Jodeiri Shokri, B.; Nourizadeh, H.; Taheri, A. Analysing Double Shearing Mechanism in Fiberglass Rock Bolting Systems: A Comprehensive Analytical Model and Numerical Simulation Approach. *Geotech. Geol. Eng.* **2024**, *42*, 7339–7370.
45. Itasca Consulting Group, Inc. *Itasca*, version 7.0; 3DEC—Three-Dimensional Distinct Element Code; Itasca Consulting Group, Inc.: Minneapolis, MN, USA, 2024.
46. Entezam, S.; Jodeiri Shokri, B.; Nourizadeh, H.; Gregor, P.; Entezam, A.; Mirzaghorbanali, A.; McDougall, K.; karunasena, W.; Aziz, N. Investigating the axial and shear performance of fiberglass rock bolts. In *Proceedings of the Resource Operators Conference*; University of Wollongong: Wollongong, Australia, 2024.
47. Zheng, H.; Jiang, Y.; Zhang, S.; Wu, X.; Chen, H. Comparative study of shear performance of fully-grouted and energy-absorbing bolts under varying normal stress during cyclic shear tests. *Bull. Eng. Geol. Environ.* **2025**, *84*, 1–14.
48. Khaleghparast, S.; Aziz, N.; Remennikov, A.; Anzanpour, S. An experimental study on shear behaviour of fully grouted rock bolt under static and dynamic loading conditions. *Tunn. Undergr. Space Technol.* **2023**, *132*, 104915.
49. Aziz, N.; Nemcik, J.; Mirzaghorbanali, A.; Foldi, S.; Joyce, D.; Moslemi, A.; Ghojavand, H.; Ma, S.; Li, X.; Rasekh, H. Suggested methods for the preparation and testing of various properties of resins and grouts. In *Proceedings of the Coal Operators' Conference*; University of Wollongong: Wollongong, Australia, 2014.
50. Yu, J.-D.; Lee, J.-S.; Tamang, B.; Park, S.; Chang, S.; Kim, J.; Kim, Y. Performance Evaluation of GFRP Rock Bolt Sensor for Rock Slope Monitoring by Double Shear Test. *Adv. Civ. Eng.* **2020**, *2020*, 1–14.
51. Hosseini, S.; Entezam, S.; Jodeiri Shokri, B.; Mirzaghorbanali, A.; Nourizadeh, H.; Motallebiyan, A.; Entezam, A.; McDougall, K.; Karunasena, W.; Aziz, N. Predicting grout's uniaxial compressive strength (UCS) for fully grouted rock bolting system by applying ensemble machine learning techniques. *Neural Comput. Appl.* **2024**, *36*, 18387–18412.
52. Gao, H.; Wang, Q.; Jiang, B.; Zhang, P.; Jiang, Z.; Wang, Y. Relationship between rock uniaxial compressive strength and digital core drilling parameters and its forecast method. *Int. J. Coal Sci. Technol.* **2021**, *8*, 605–613.
53. Beiki, M.; Majdi, A.; Givshad, A.D. Application of genetic programming to predict the uniaxial compressive strength and elastic modulus of carbonate rocks. *Int. J. Rock Mech. Min. Sci.* **2013**, *63*, 159–169.

54. Hong, S.; Park, S.-K. Uniaxial Bond Stress-Slip Relationship of Reinforcing Bars in Concrete. *Adv. Mater. Sci. Eng.* **2012**, *2012*, 1–12.
55. A.J. Hyett; W.F. Bawden; R.D. Reichert. The effect of rock mass confinement on the bond strength of fully grouted cable bolts. *Int. J. Rock Mech. Min. Sci. Geomech. Abstr.* **1992**, *29*, 503–524.
56. Yazici, S.; Kaiser, P.K. Bond strength of grouted cable bolts. *Int. J. Rock Mech. Min. Sci. Geomech. Abstr.* **1992**, *29*, 279–292.
57. Zhao, T.-b.; Guo, W.-y.; Yin, Y.-c.; Tan, Y.-l. Bolt Pull-Out Tests of Anchorage Body under Different Loading Rates. *Shock Vib.* **2015**, *2015*, 1–8.
58. Chen, J.; Wang, S.; Sun, G.; Zhang, H.; Skrzypkowski, K.; Zagórski, K.; Zagórska, A. Investigating the Influence of Embedment Length on the Anchorage Force of Rock Bolts with Modified Pile Elements. *Appl. Sci.* **2022**, *13*, 52.
59. Itasca Consulting Group, Inc. (2024) *3DEC — Three-Dimensional Distinct Element Code, Ver. 7.0*. Minneapolis: Itasca..
60. Chang, L.; Konietzky, H. Application of the Mohr-Coulomb Yield Criterion for Rocks with Multiple Joint Sets Using Fast Lagrangian Analysis of Continua 2D (FLAC2D) Software. *Energies* **2018**, *11*, 614.

Disclaimer/Publisher's Note: The statements, opinions and data contained in all publications are solely those of the individual author(s) and contributor(s) and not of MDPI and/or the editor(s). MDPI and/or the editor(s) disclaim responsibility for any injury to people or property resulting from any ideas, methods, instructions or products referred to in the content.